Supplementary Information

Solar and thermal dual-band electrochromic windows for energy-efficient buildings

Jian Chen[1, 2†], Jianwei Hu[1, 2†], Banghai Wang[2], Huajie Zhang[1, 2], Jie Liang[2], Peiru Shi[2], Jia Zhu[1, 2*], Yan Jin[1*]

[1]National Laboratory of Solid State Microstructures, School of Sustainable Energy and Resources, Frontiers Science Center for Critical Earth Material Cycling, Nanjing University, Suzhou, 215163, P. R. China

[2]College of Engineering and Applied Sciences, Collaborative Innovation Center of Advanced Microstructures, Jiangsu Key Laboratory of Artificial Functional Materials, Nanjing University, Nanjing, 210093, P. R. China

† These authors contributed equally to this work

* Corresponding authors. E-mails: jiazhu@nju.edu.cn; yanjin@nju.edu.cn

Supplementary Figures

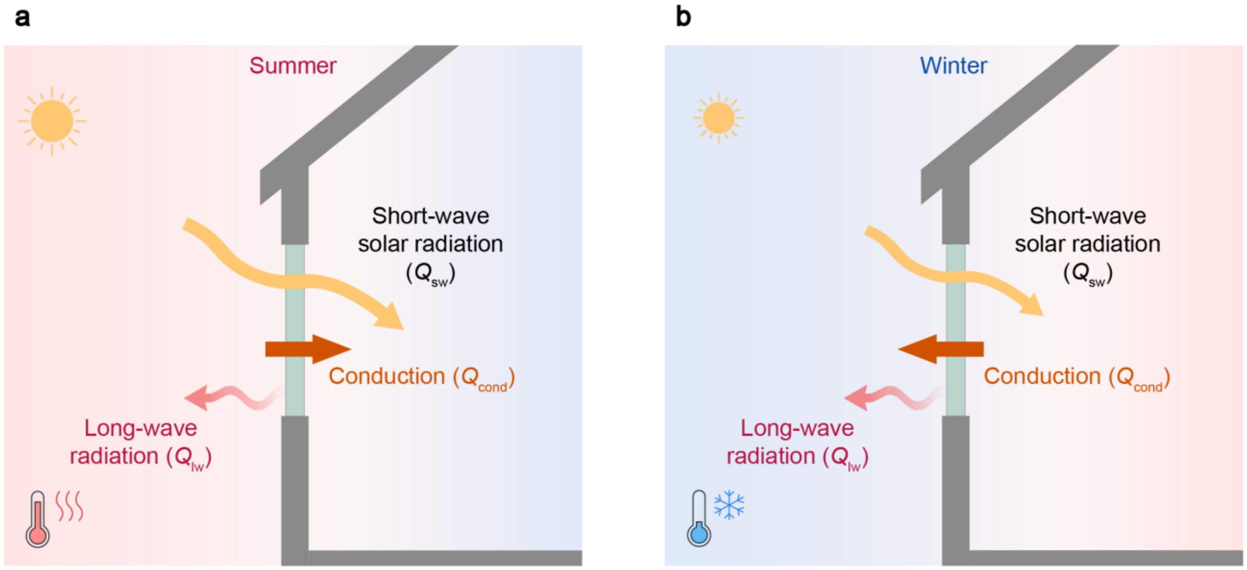

Supplementary Fig. 1: Schematic of heat transfer across conventional single-glazed windows (excluding convection effects). **a**, Summer conditions. **b**, Winter conditions.

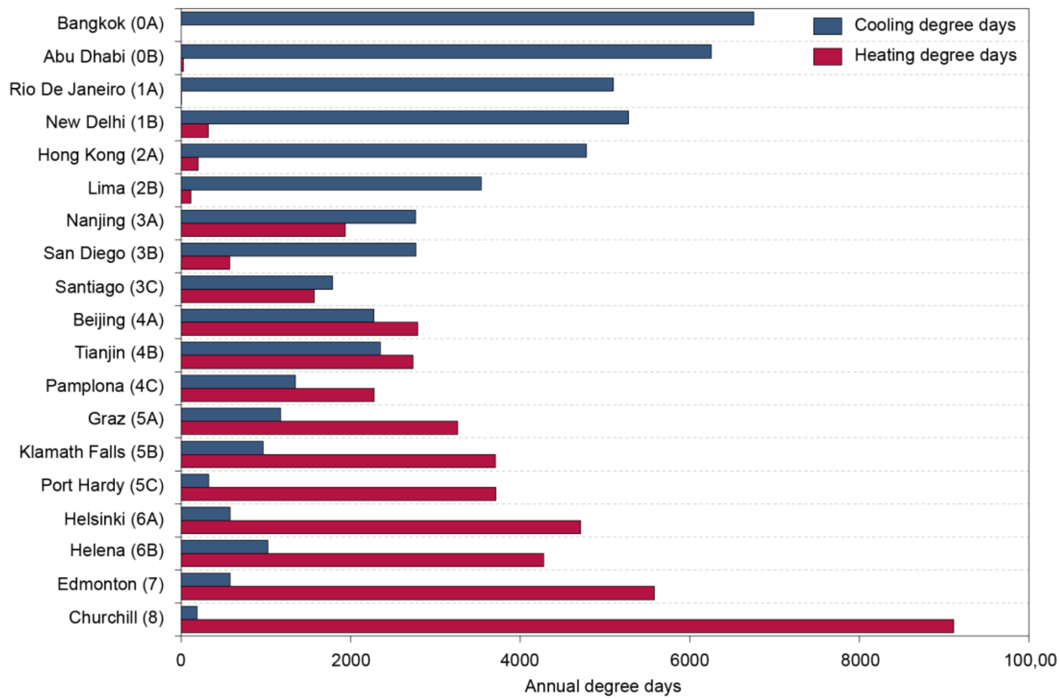

Supplementary Fig. 2: Yearly heating and cooling degree days of 19 cities worldwide, each representing one of the 19 climate zones. It can be found most cities need both heating and cooling throughout the whole year.

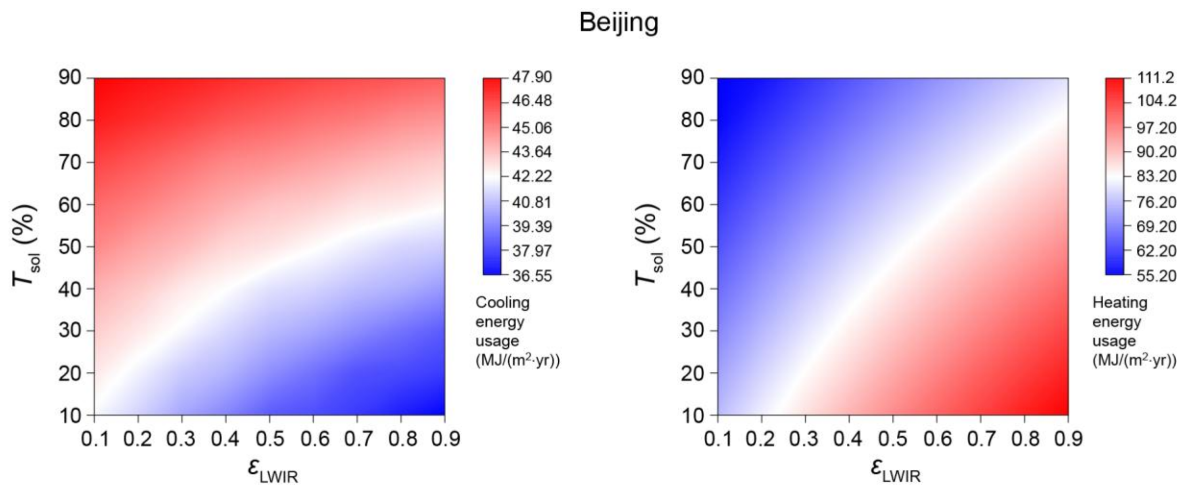

Supplementary Fig. 3: Cooling (left) and heating (right) energy consumption mapping in Beijing with varied T_{sol} and ε_{LWIR}. The lowest energy usage for cooling is observed at ε_{LWIR} = 0.9 and T_{sol} = 10%, whereas the least energy usage for heating occurs at ε_{LWIR} = 0.1 and T_{sol} = 90%. This highlights the significance of dynamic dual-band regulation of T_{sol} (0.38–2.5 μm) and ε_{LWIR} (2.5–20 μm) through windows for achieving energy-efficient buildings.

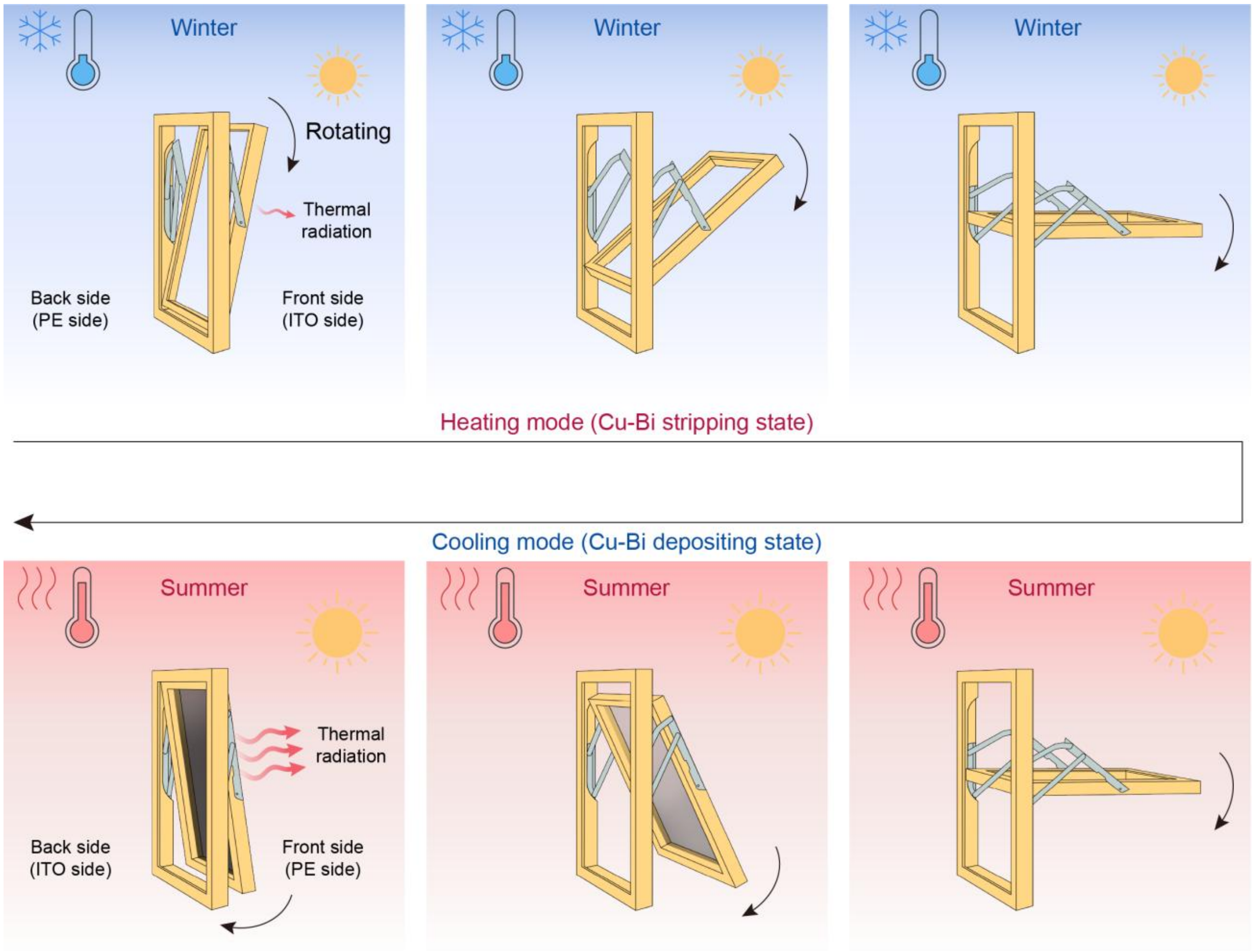

Supplementary Fig. 4: Schematic of occupant-friendly mechanically-assisted rotating operation of the STDEC window.

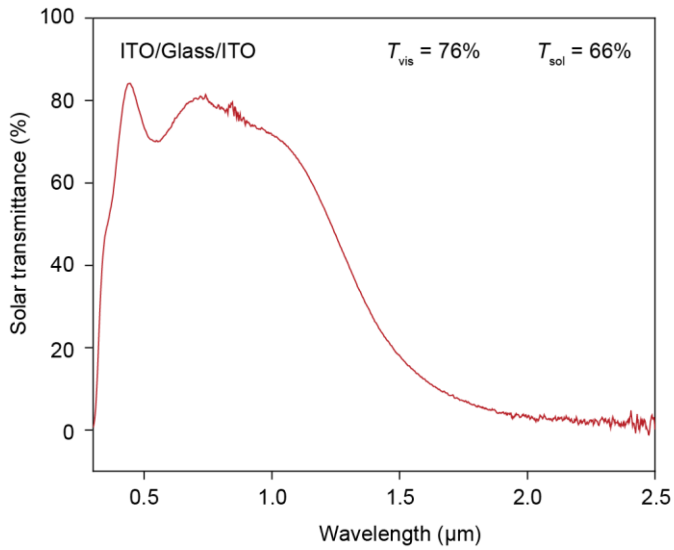

Supplementary Fig. 5: The solar transmittance spectrum of double-sided ITO conductive glass shows a T_{vis} of up to 76% and a T_{sol} of up to 66%.

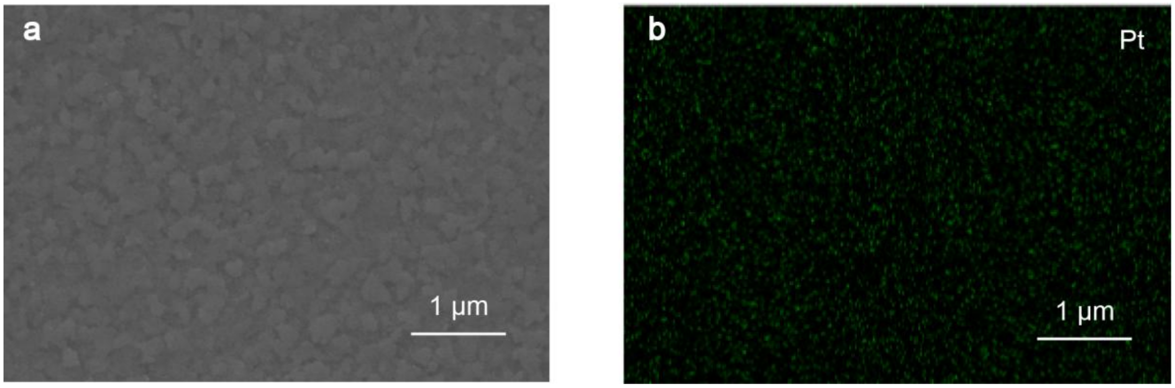

Supplementary Fig. 6: SEM image and EDS mapping of the ITO modified with Pt nanoparticles.

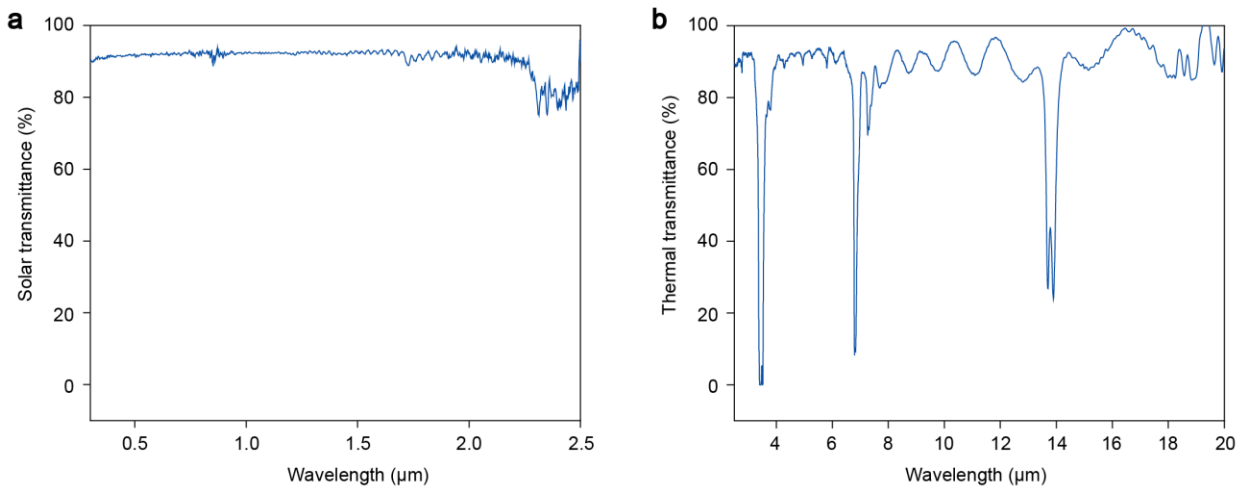

Supplementary Fig. 7: Transmittance spectra of PE membrane ranging from 0.3 to 20 μm.

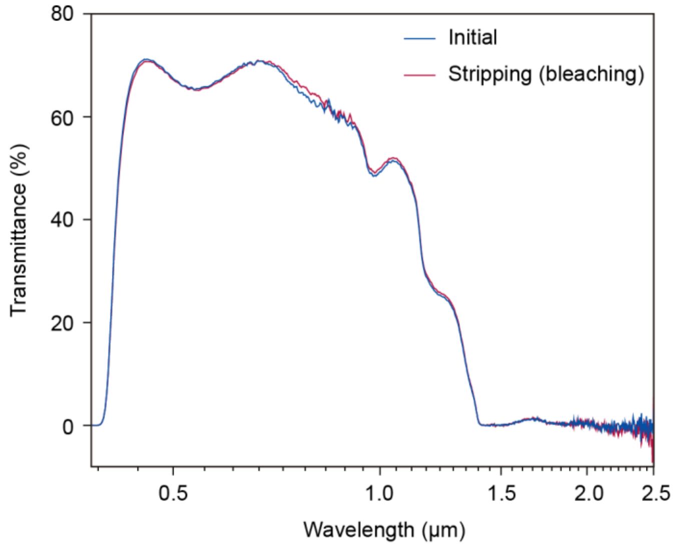

Supplementary Fig. 8: Transmittance spectra of the STDEC window in the solar range (0.38–2.5 μm) for both the initial and bleached states, respectively. The solar transmittance returns to its initial state value through the complete bleaching of the Cu–Bi film.

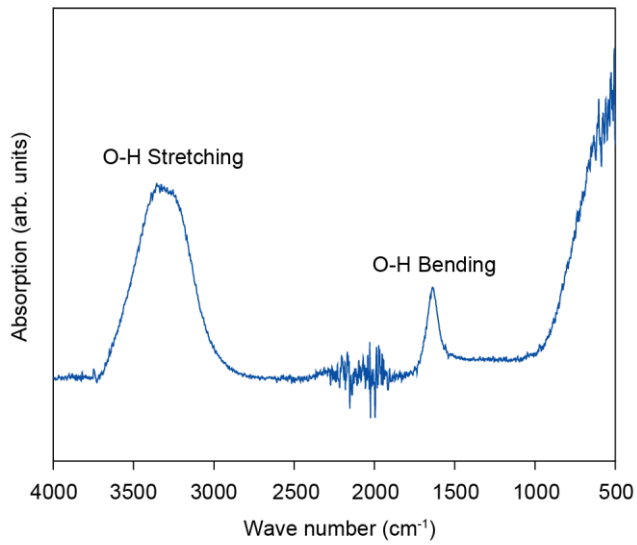

Supplementary Fig. 9: Fourier-transform infrared spectroscopy of the aqueous Cu–Bi electrolyte.

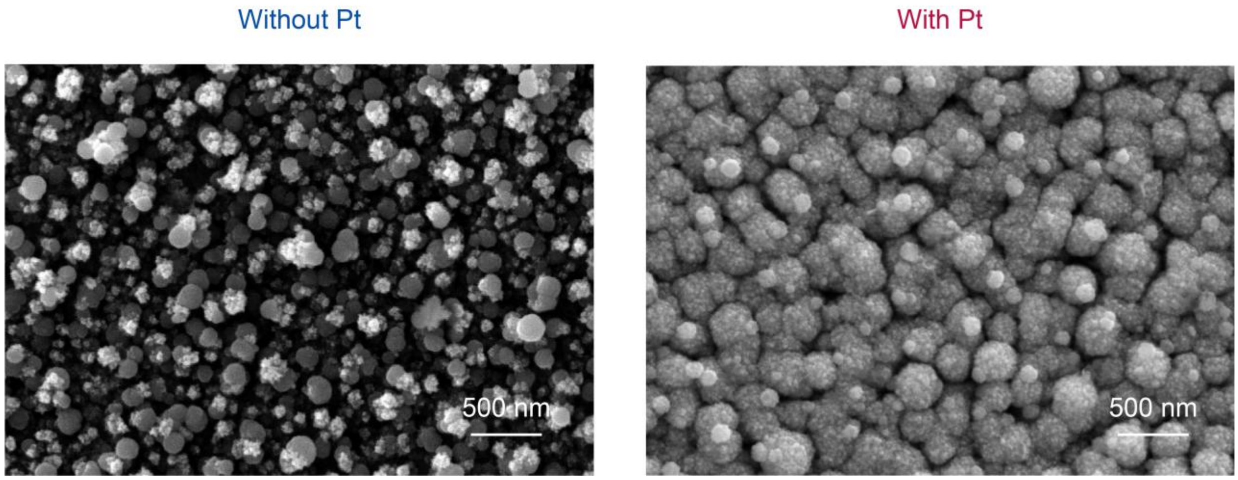

Supplementary Fig. 10: SEM images of the deposited Cu–Bi films on ITO substrates without and with Pt nanoparticle modification. The Cu–Bi films lacking Pt nanoparticles exhibit a rough, porous, and uneven surface morphology, whereas the films that include Pt nanoparticles display a dense and uniform morphology with extensive surface coverage.

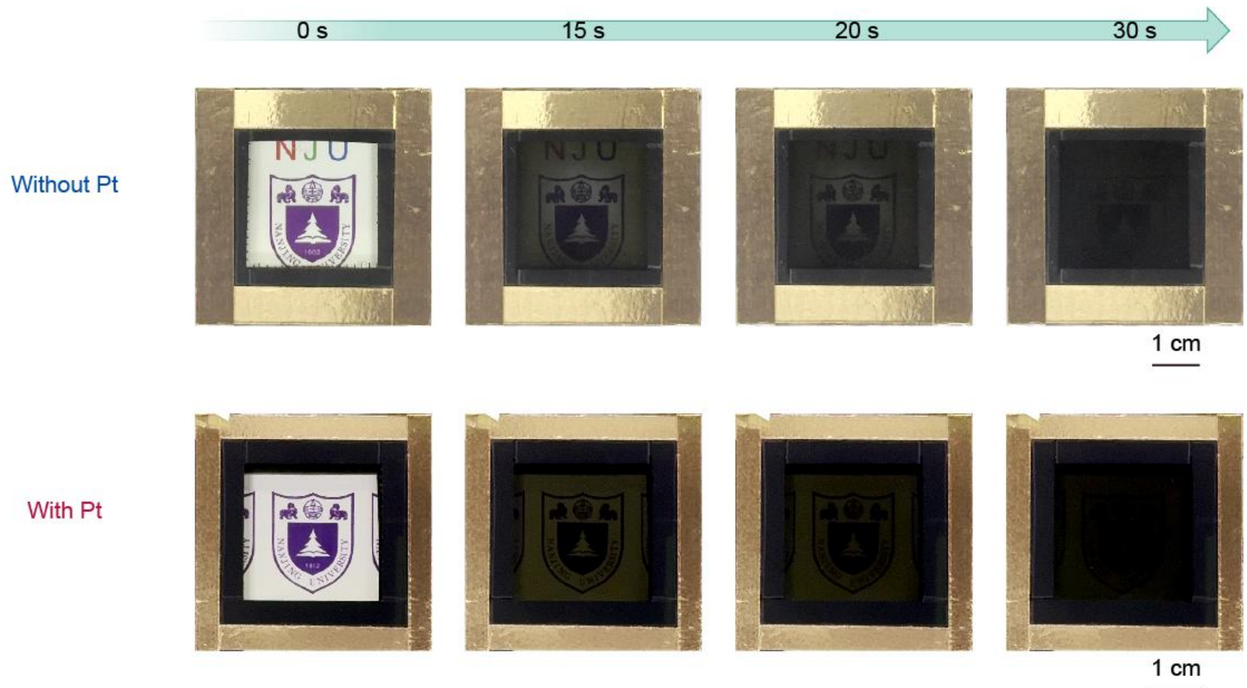

Supplementary Fig. 11: Optical images of the Cu–Bi film deposition processes reveal differences between those without and with Pt nanoparticle modification. The former exhibit irregular deposition and color variations, while the latter demonstrate a uniform deposition and consistent coloration in a 25 cm^2 device.

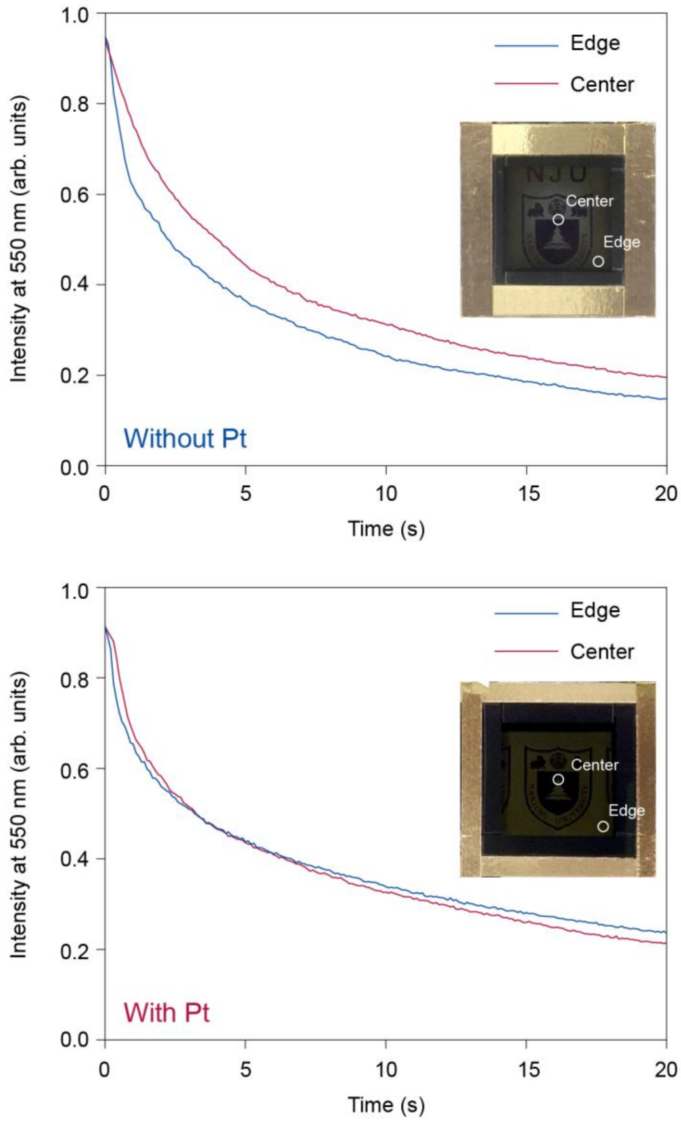

Supplementary Fig. 12: Transmission at 550 nm through the edge and the center of the 25 cm^2 windows, without and with the modification of Pt nanoparticles.

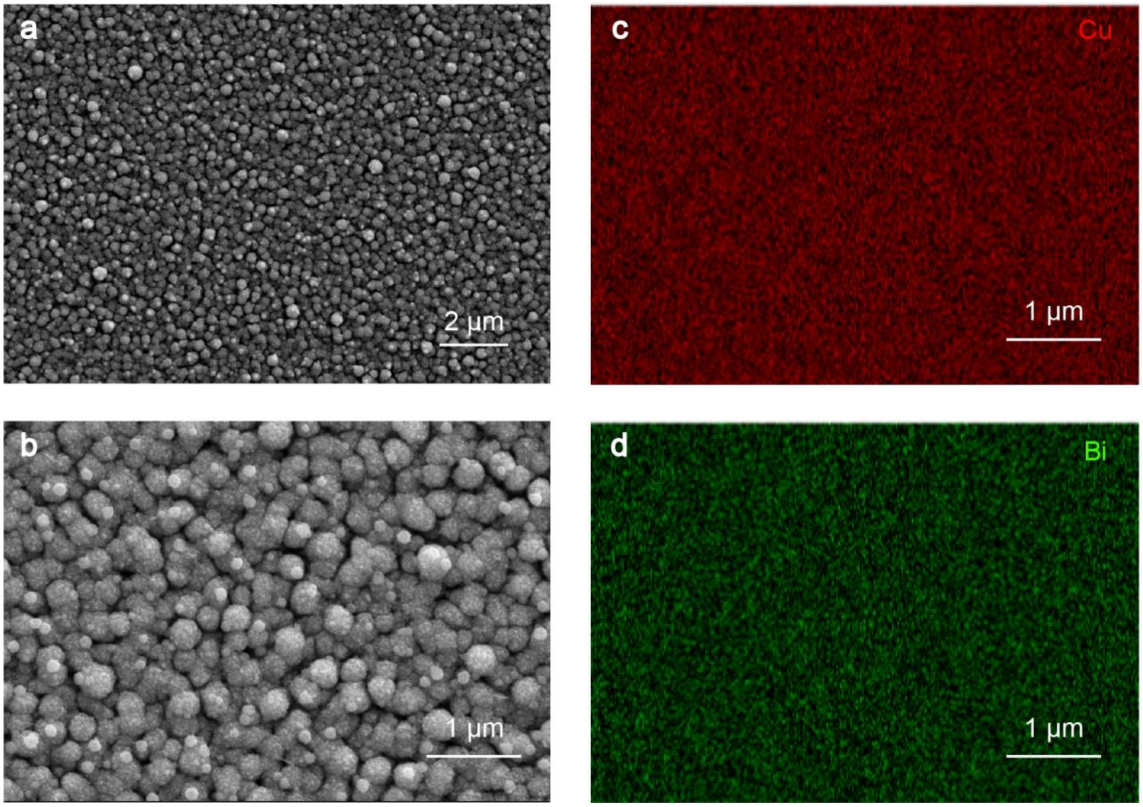

Supplementary Fig. 13: SEM images and corresponding EDS maps of the deposited Cu–Bi films on Pt nanoparticle modified ITO substrate.

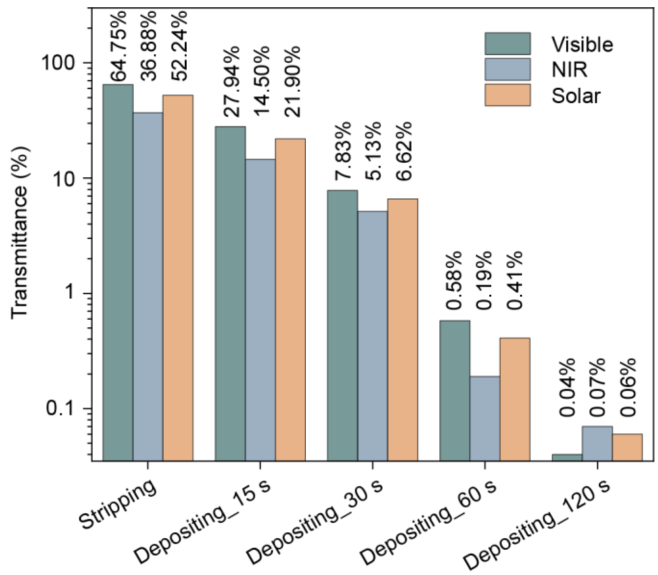

Supplementary Fig. 14: The weighted average transmittance of visible (T_{vis}, 0.38–0.78 μm), near-infrared (T_{NIR}, 0.78–2.5 μm), and solar spectrum (T_{sol}, 0.38–2.5 μm) at different deposition times. The STDEC window demonstrates time-dependent T_{vis} and T_{sol} values below 1.0% after 60 s of deposition, and under 0.1% after 120 s.

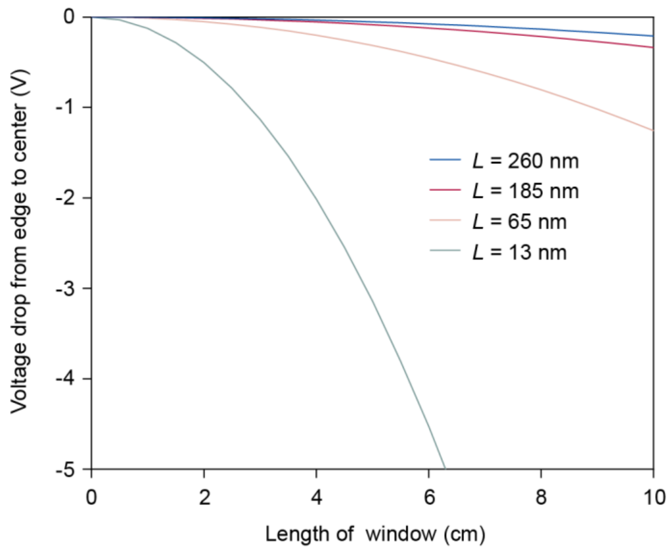

Supplementary Fig. 15: The sheet resistance (thickness dependent) of the ITO working electrode on voltage drop for uniform deposition and tinting. The equation for voltage drops across a two-dimensional electrode[1,2] is given by $\Delta V = -\left(\frac{JR_s}{2}\right)\left(\frac{L_e}{2}\right)^2$, where J is the current density (3.35 mA cm^{-2}), R_s is the sheet resistance (as presented in supplementary Table 1), and L_e is the electrode length. This indicates that lower sheet resistance (such as 5 and 8 ohm/sq at 260 and 185 nm) can reduce the voltage drop from the edge to the center of the STDEC window, facilitating uniform deposition and coloration of the Cu–Bi films in a 100 cm^2 device.

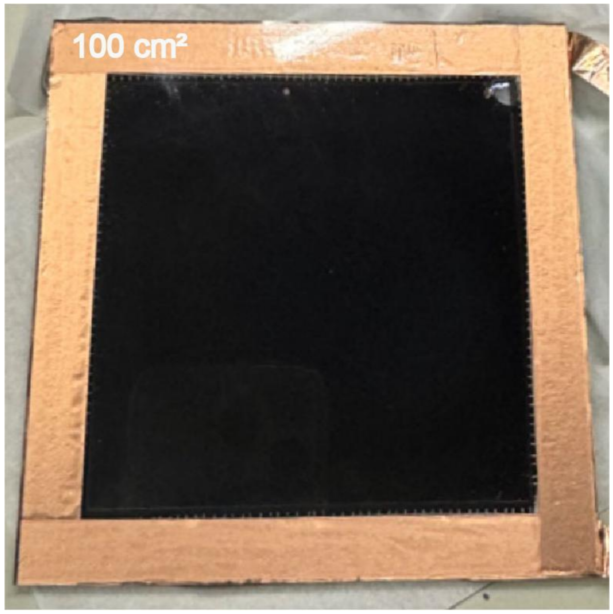

Supplementary Fig. 16: A visual representation of a 100 cm^2 STDEC window with homogeneous deposition and coloration.

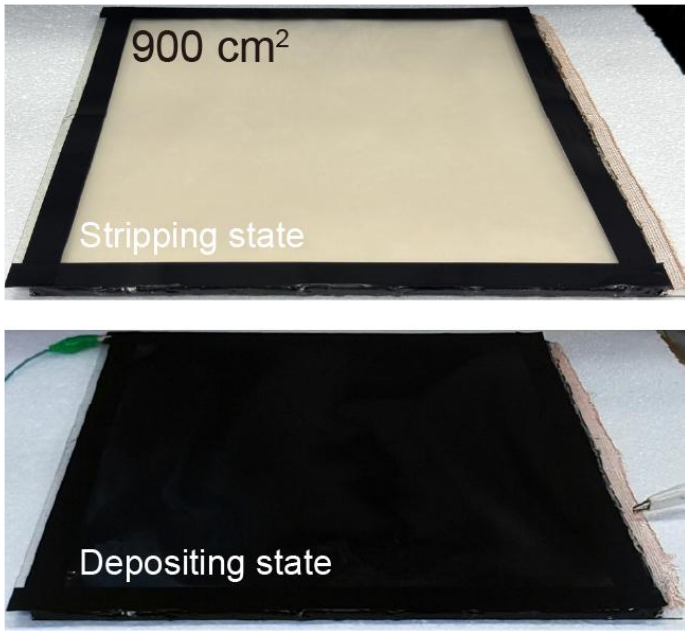

Supplementary Fig. 17: A visual representation of a 900 cm^2 STDEC window with homogeneous deposition and coloration.

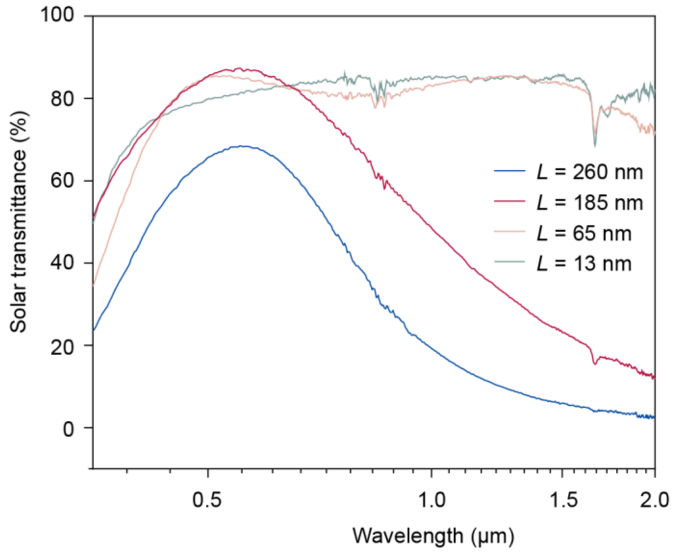

Supplementary Fig. 18: Solar transmission spectra of ITO electrodes with different thicknesses. The ITO layer, when its thickness ranges from 13 to 185 nm, demonstrates a high T_{vis} of over 80% and a high T_{sol} of 60%–80%. In contrast, an overly thick ITO layer, such as one measuring 260 nm, exhibits a low T_{vis} of around 60% and a low T_{sol} of about 40%.

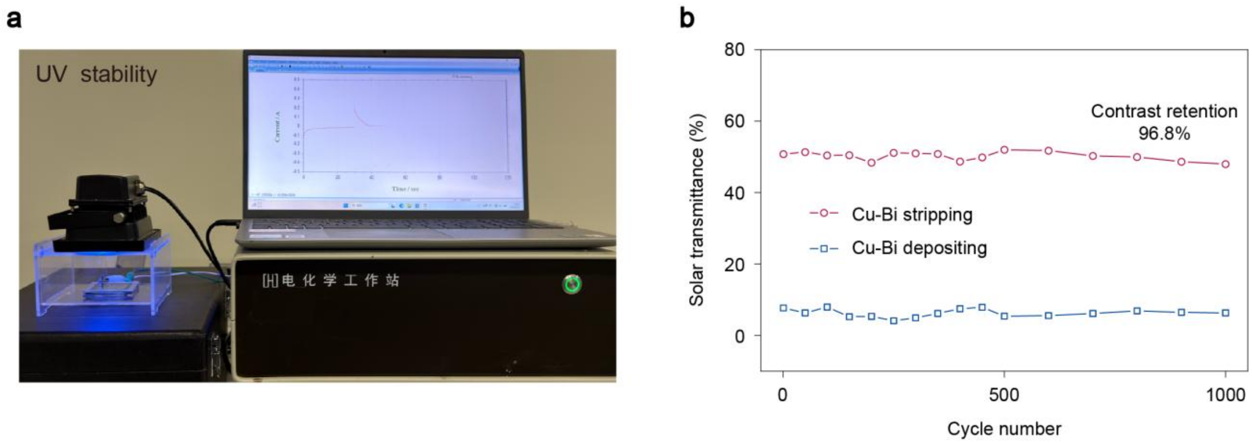

Supplementary Fig. 19: UV stability. **a**, Photograph of the experimental setup for extended UV exposure at 640 W m^{-2}. **b**, Cycling stability over 1,000 cycles, showing 96.8% retention of optical contrast.

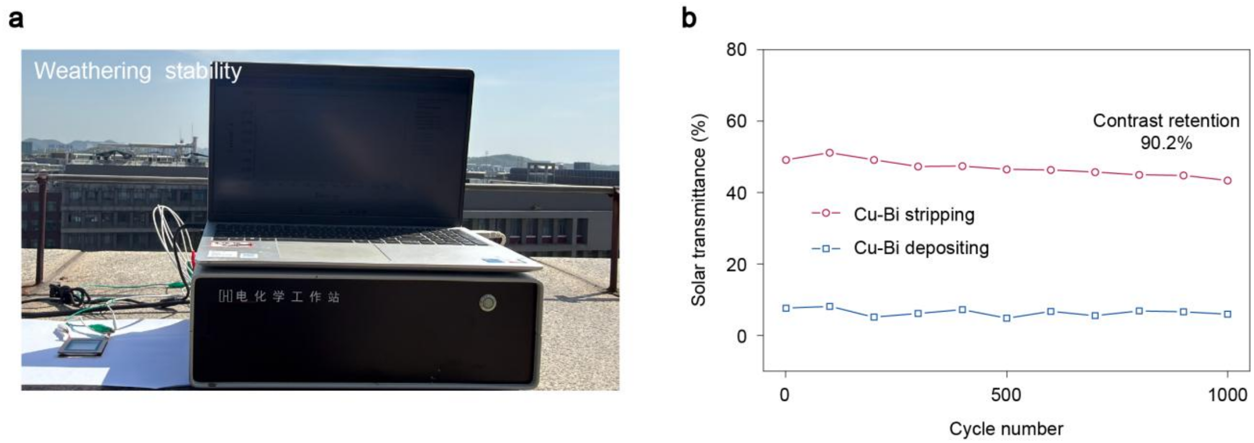

Supplementary Fig. 20: Outdoor weathering stability. **a**, Photograph of the experimental setup for outdoor weathering test. **b**, Cycling stability over 1,000 cycles, showing 90.2% retention of optical contrast.

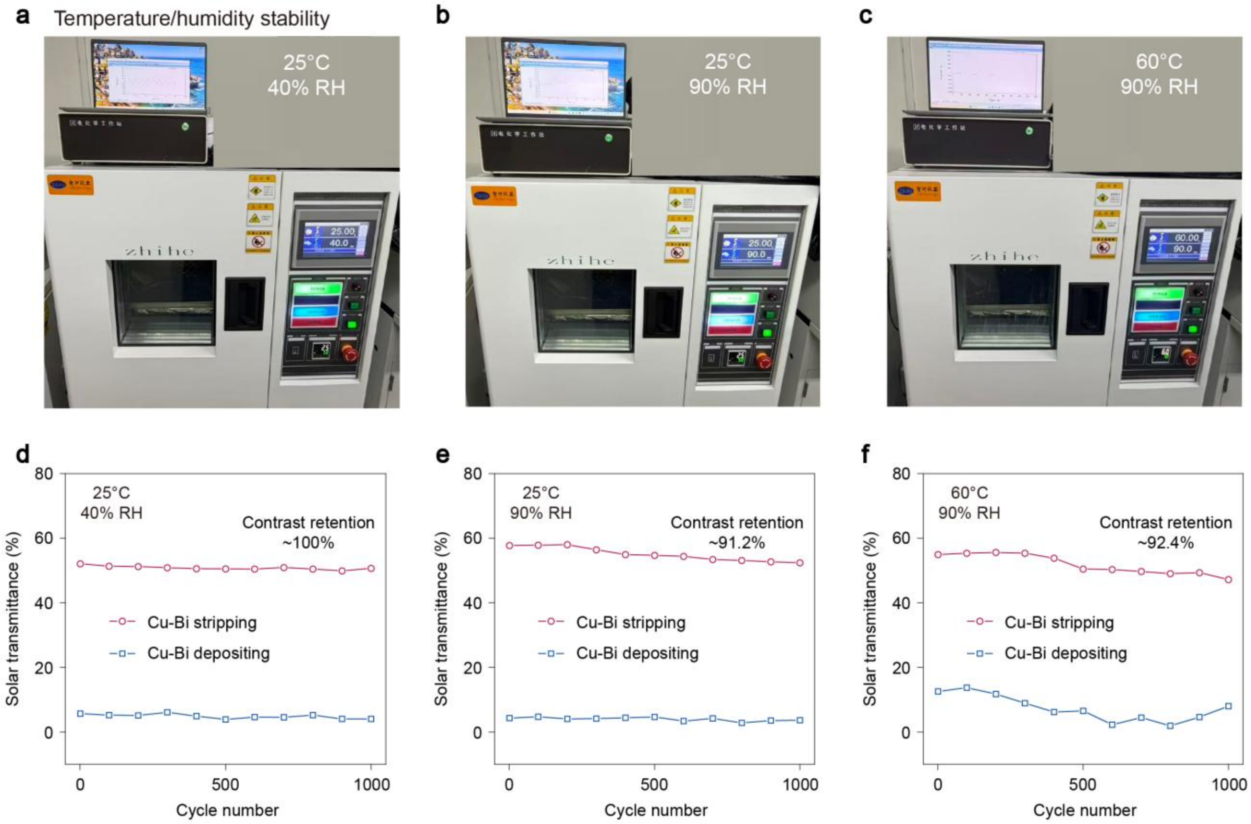

Supplementary Fig. 21: Temperature/humidity stability. **a–c**, Photographs of the experimental setup for temperature/humidity cycling tests in a constant temperature and humidity chamber under 3 conditions: 25℃/40% RH (**a**), 25℃/90% RH (**b**), and 60℃/90% RH (**c**). **d–f**, Corresponding cycling stability over 1,000 cycles, with optical contrast retention of ~100% (**d**), 91.2% (**e**), and 92.4% (**f**).

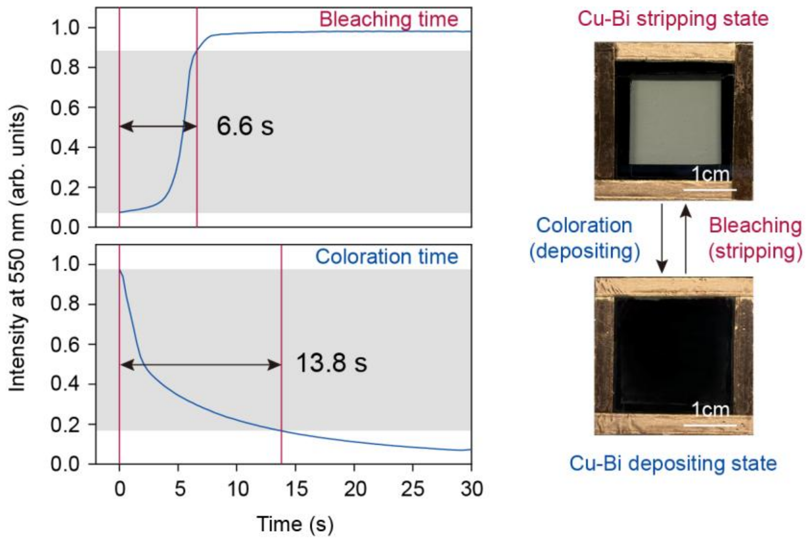

Supplementary Fig. 22: The switching times were derived from normalized transmission spectra following the standard electrochromic measurement protocol. Defined as the time required for the transmittance change at a specific wavelength to reach 90% of its total variation in response to a step voltage, the switching times measured in experiments for the ~10 cm^2 STDEC window show a bleaching time of 6.6 s for Cu–Bi stripping and a coloration time of 13.8 s for Cu–Bi depositing.

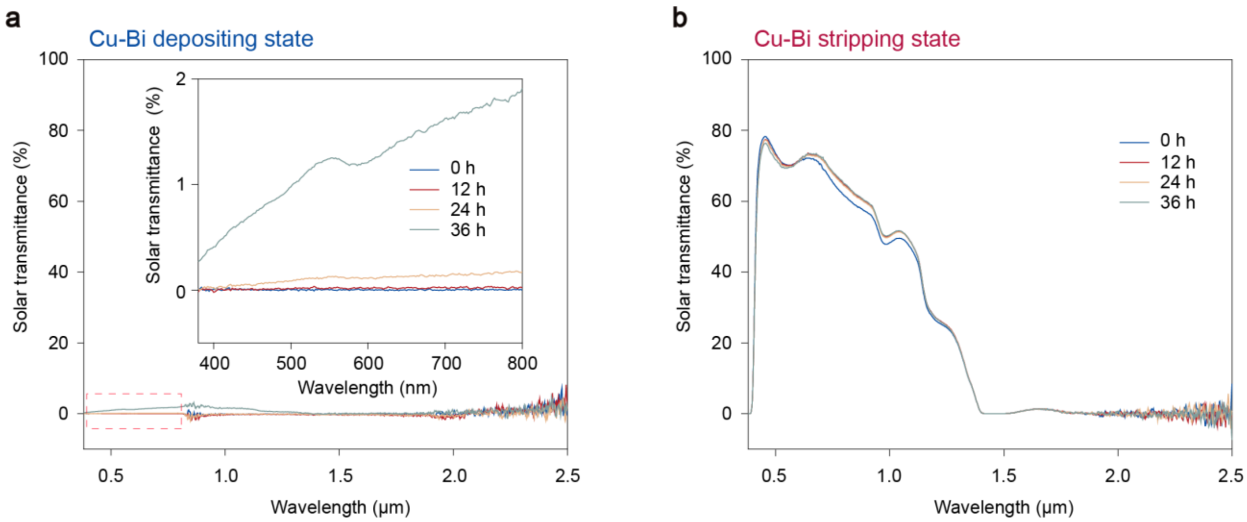

Supplementary Fig. 23: Bistability of the STDEC window. Optical monitoring of the STDEC window in the (**a**) colored (depositing) and (**b**) transparent (stripping) states were conducted under open-circuit conditions for 36 hours. Excellent bistability is observed, with an optical loss of less than 2% in the colored state and no measurable loss in the transparent state.

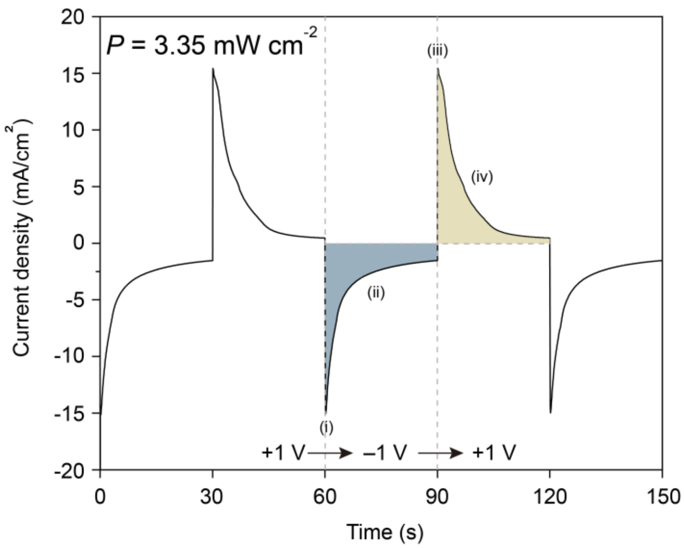

Supplementary Fig. 24: Chronoamperometric curve of the STDEC window. The current–time curve shows the distinct stages of the Cu–Bi film deposition and stripping: (i) instantaneous nucleation of Cu–Bi clusters; (ii) concurrent nucleation and growth; (iii, iv) stripping and dissolution of the Cu–Bi film. These symmetric peaks (charge ~100.5 mC/cm^2) indicate excellent electrochemical reversibility and stable cycling performance, with an average power consumption of 3.35 mW cm^{-2}.

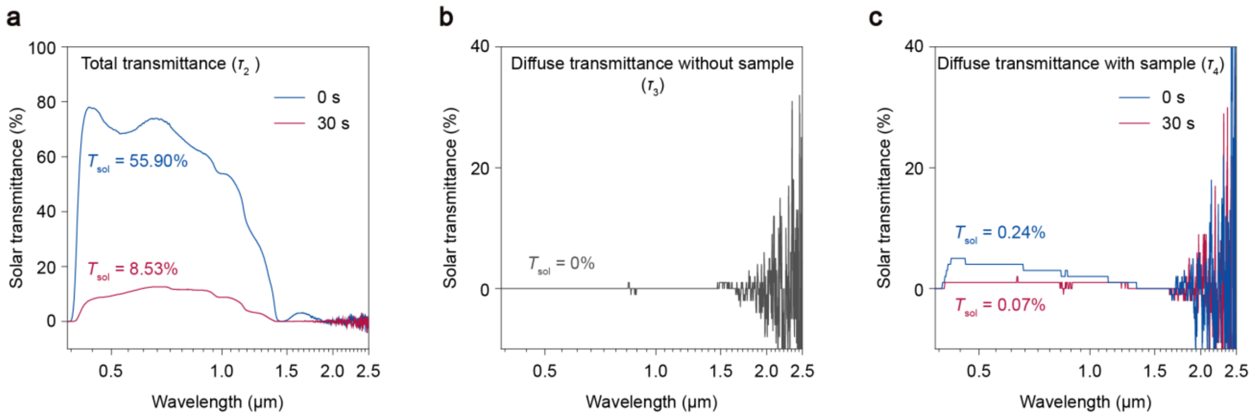

Supplementary Fig. 25: Haze calculation of the STDEC window. **a**, Total transmittance spectra of the STDEC window in the stripping and depositing states. **b**, Diffuse transmittance spectrum measured without the window sample. **c**, Diffuse transmittance spectra of the STDEC window in the stripping and depositing states.

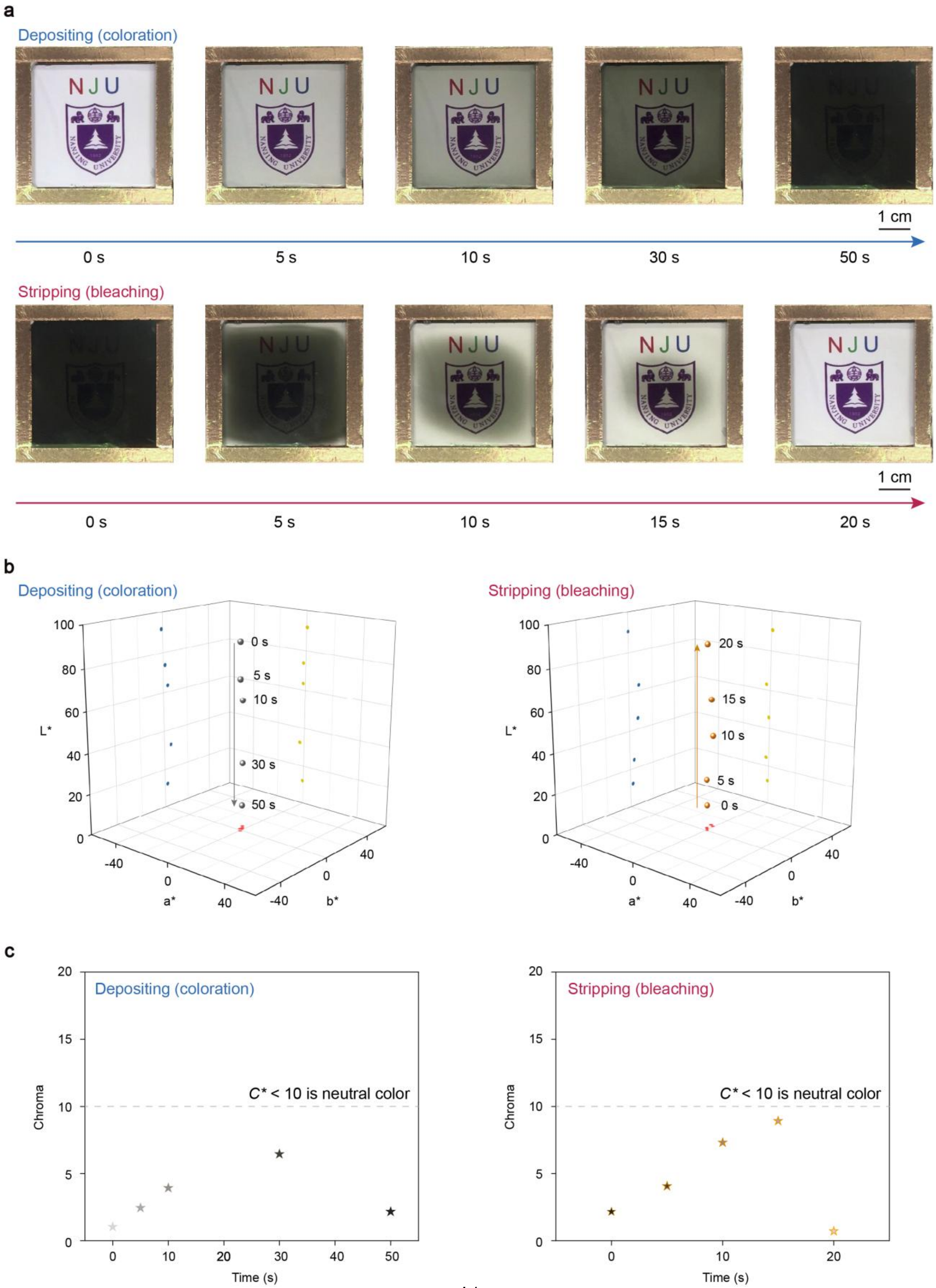
a
Depositing (coloration)
NJU
1 cm
0 s
5 s
10 s
30 s
50 s
Stripping (bleaching)
1 cm
0 s
5 s
10 s
15 s
20 s
b
Depositing (coloration)
0 s
5 s
10 s
30 s
50 s
L*
a*
b*
Stripping (bleaching)
20 s
15 s
10 s
5 s
0 s
L*
a*
b*
c
Depositing (coloration)
C* < 10 is neutral color
Chroma
Time (s)
Stripping (bleaching)
C* < 10 is neutral color
Chroma
Time (s)

Supplementary Fig. 26: Color neutrality characterization of the STDEC window. **a**, Optical photographs of a 25 cm^2 STDEC window during the Cu–Bi depositing (coloration) and stripping (bleaching) processes, illustrating a neutral color transition (clear-to-grey-to-black) throughout the RME process. **b**, $L^*a^*b^*$ coordinates for various optical states at different depositing and stripping times. **c**, The color neutrality is characterized by the chroma (C^*) value in the CIE $L^*a^*b^*$ color space. If C^* is below 10, the STDEC window displays a neutral color across its full optical state range during the RME process.

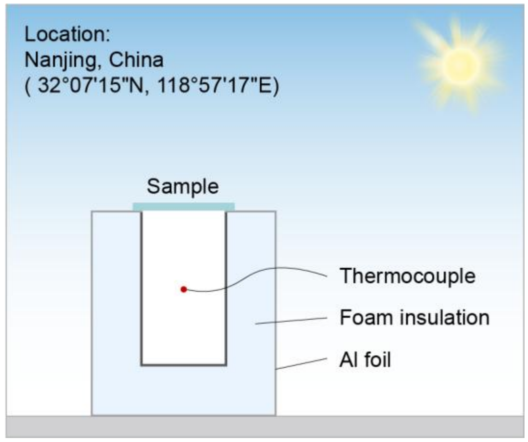

Supplementary Fig. 27: Schematic of the horizontal measurement chamber. This chamber was constructed from polystyrene foam for thermal insulation. The exterior was covered with Al foil to reduce sunlight absorption. Thermocouples were placed at the center of the chambers to allow for continuous real-time monitoring of temperature.

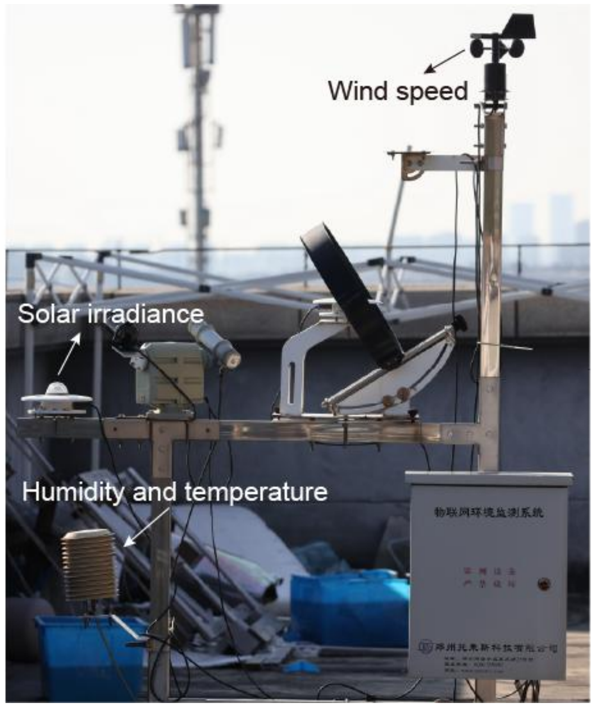

Supplementary Fig. 28: A weather station located on roof of platform monitors solar irradiance, ambient temperature, relative humidity, and wind speed.

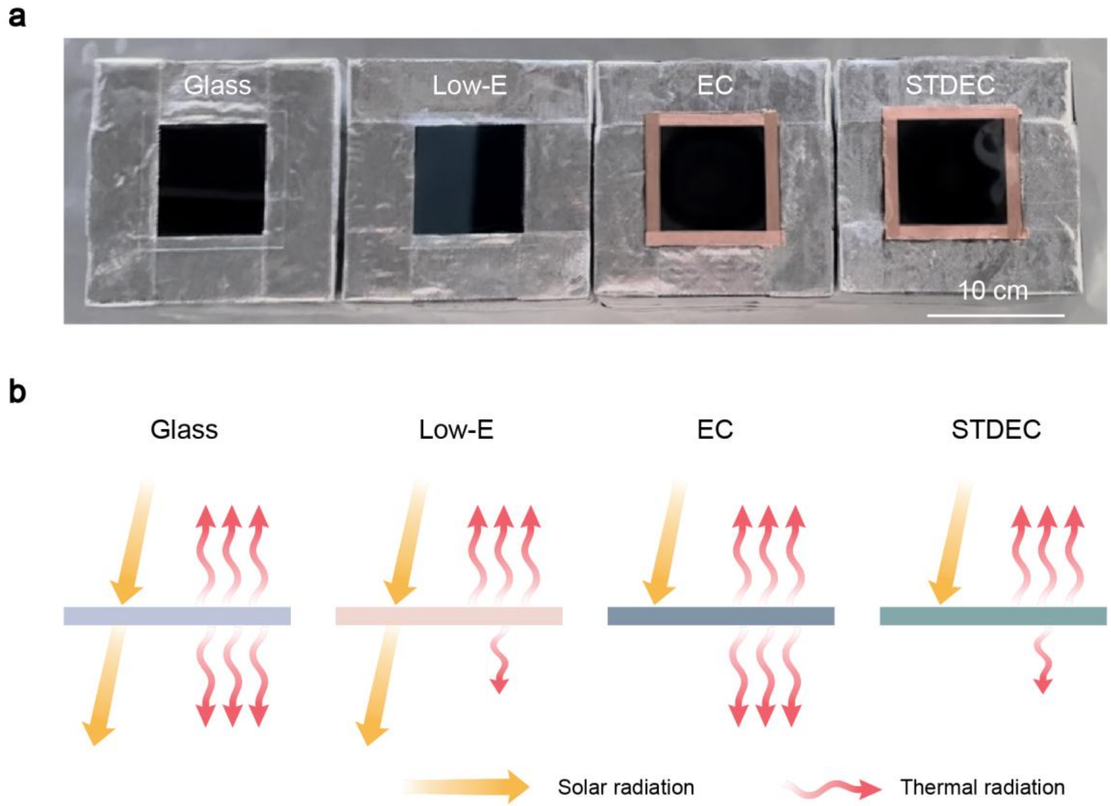

Supplementary Fig. 29: Four window samples measured in summer. **a**, A magnified top-view of horizontally oriented samples (including normal glass, low-E glass, black EC window, and black STDEC window; 100 cm^2 in size) for outdoor thermal measurement in hot summer. **b**, Emissivity design of the STDEC window and other reference samples. The STDEC window has a high front emissivity for radiative cooling heat dissipation and a low back emissivity to reduce secondary thermal radiation. In addition, the STDEC window effectively blocks solar radiation, suggesting its excellent cooling performance in the hot weather.

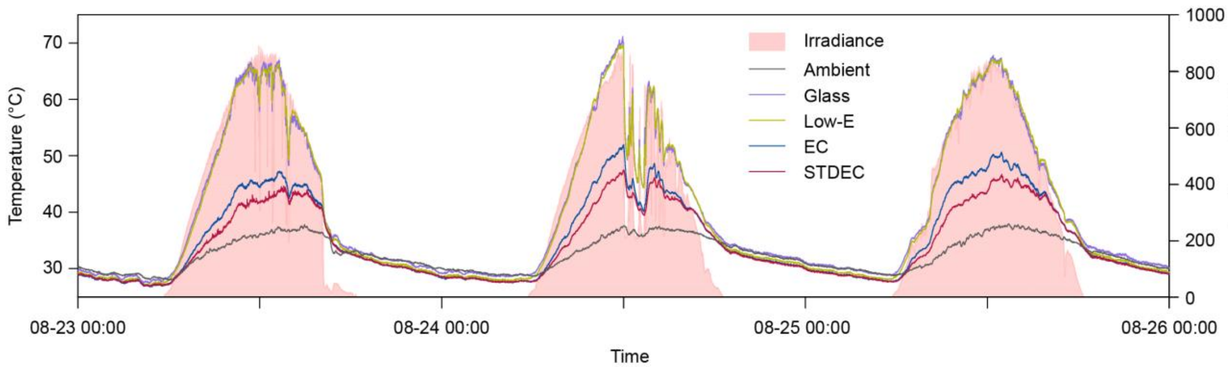

Supplementary Fig. 30: Window temperatures, ambient air temperature, and solar irradiance, measured in Nanjing over 72 continuous hours from 23 to 25 August 2024.

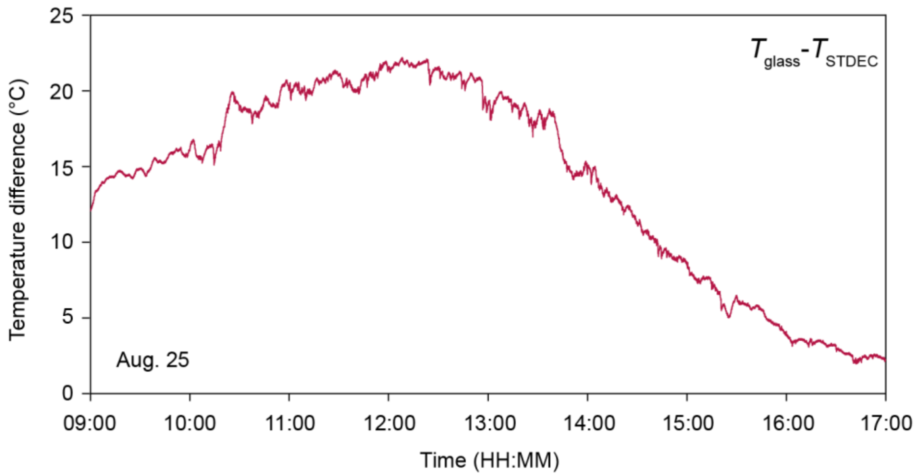

Supplementary Fig. 31: Differences in the indoor air temperatures between the two testing chambers using normal glass and STDEC window.

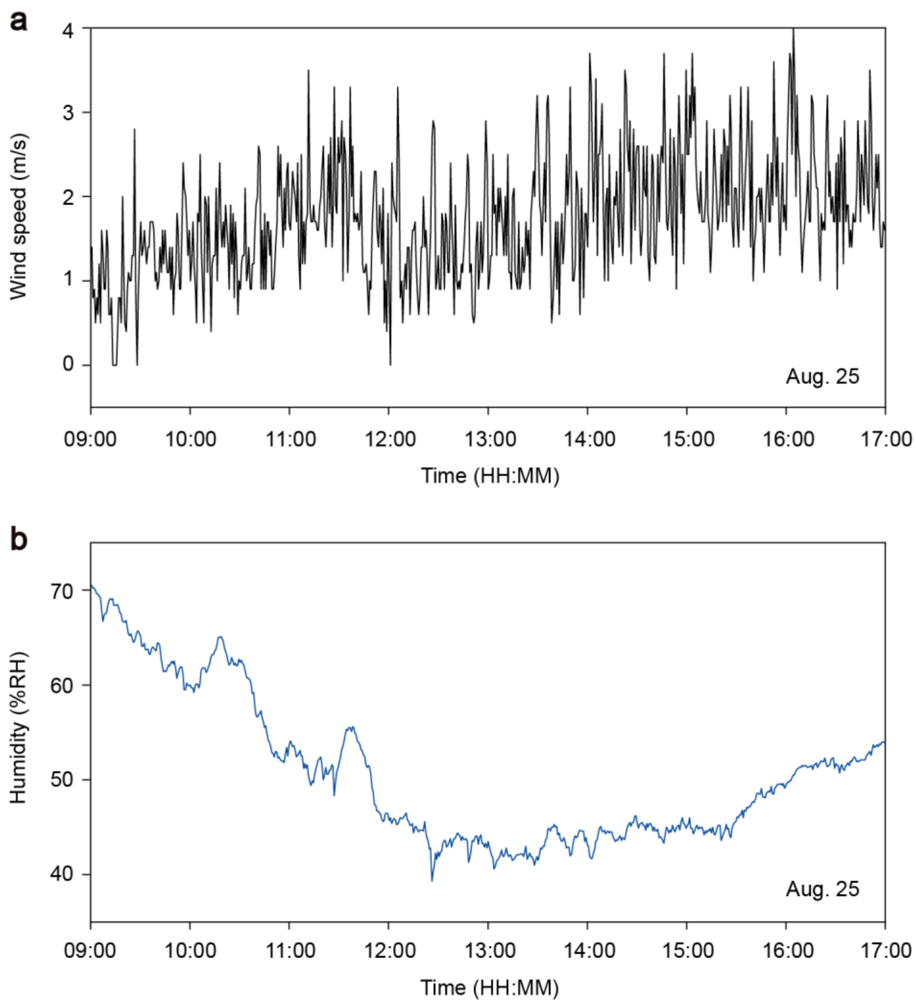

Supplementary Fig. 32: Wind speed and relative humidity recorded in Nanjing from 9:00 to 17:00 on 25 August 2024.

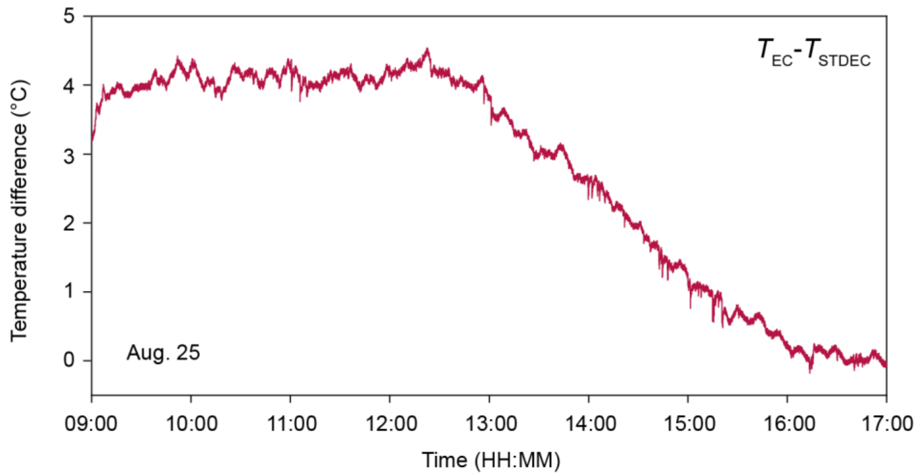

Supplementary Fig. 33: Differences in the indoor air temperatures between the two testing chambers using standard RME-based EC window and STDEC window.

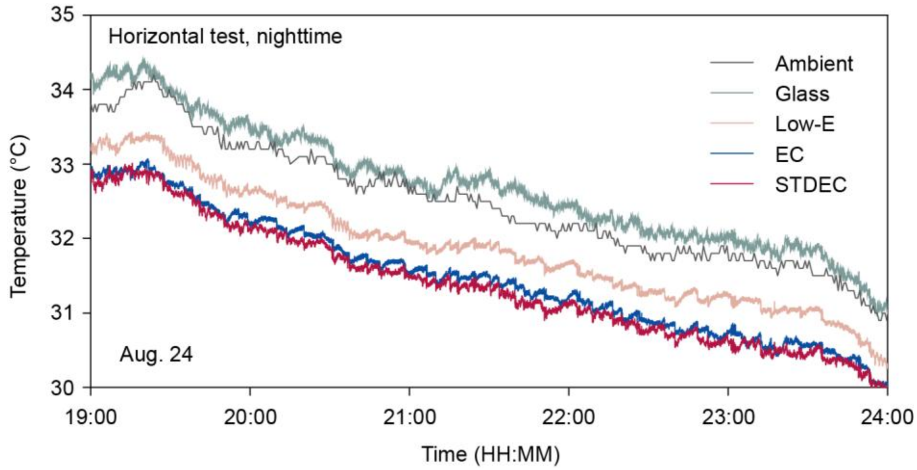

Supplementary Fig. 34: Window sample temperatures and the ambient air temperature monitored in Nanjing at night (19:00 to 24:00) on 24 August 2024. The STDEC window was found to be 1.3°C cooler than the ambient temperature of 31.9°C and 1.5°C cooler than the normal glass temperature of 32.1°C, respectively.

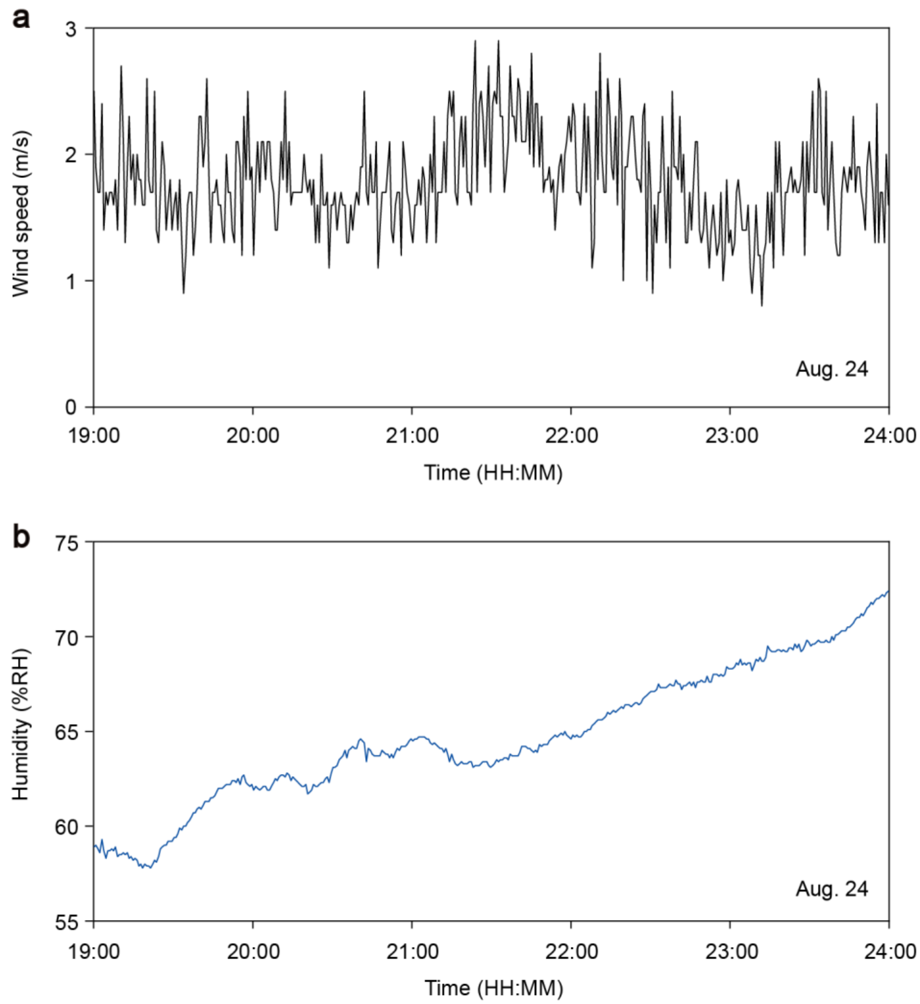

Supplementary Fig. 35: Wind speed and relative humidity recorded in Nanjing at night (19:00 to 24:00) on 24 August 2024.

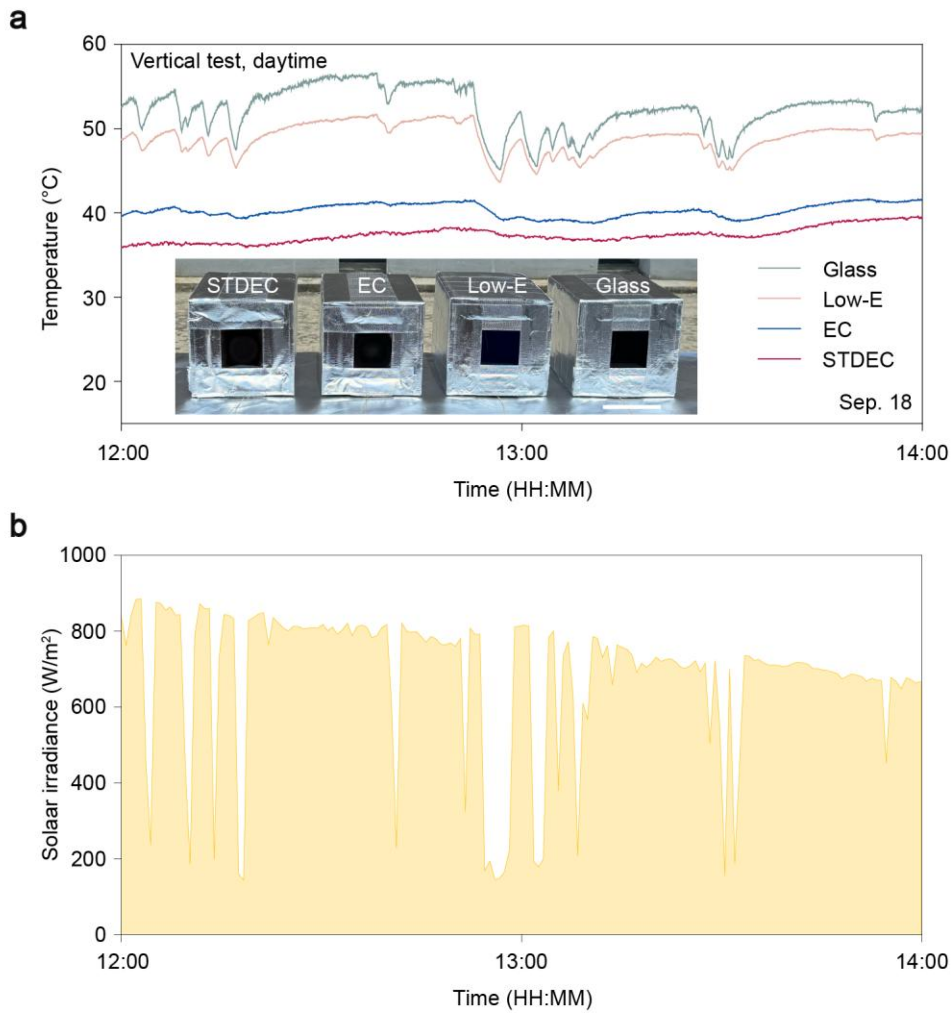

Supplementary Fig. 36: Vertical temperature measurements. **a**, Temperature tracking of different vertically oriented samples measured from 12:00 to 14:00 on 18 September 2024. The inset is an apparatus photograph showing the measurement setup for vertically oriented samples. Scale bars, 10 cm. **b**, Solar irradiance from 12:00 to 14:00 on 18 September 2024.

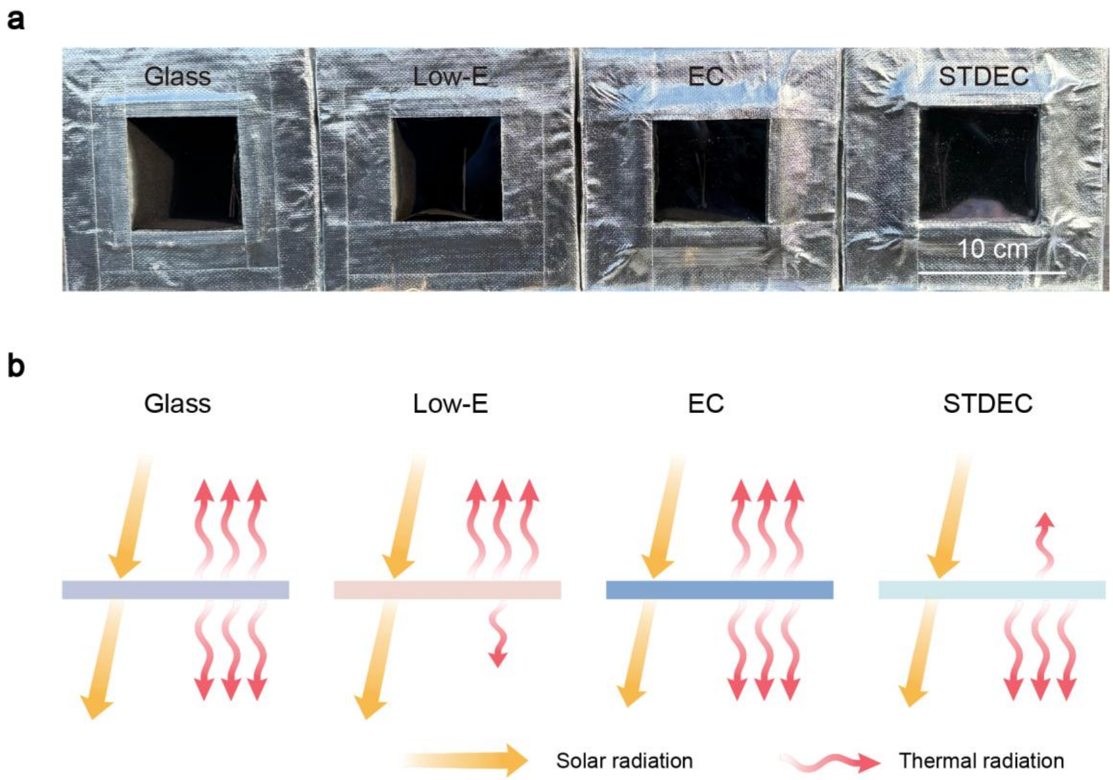

Supplementary Fig. 37: Window samples measured in winter. **a**, A magnified top-view of horizontally oriented samples (including normal glass, low-E glass, clear EC window and clear STDEC window; 100 cm^2 in size) for outdoor thermal measurement in cold winter. **b**, Emissivity design of the STDEC window and other reference samples. The STDEC window has a low front emissivity that reduces heat loss from the interior, providing effective thermal insulation. Moreover, its high transmission of solar radiation highlights its exceptional performance in capturing solar heat in the cold weather.

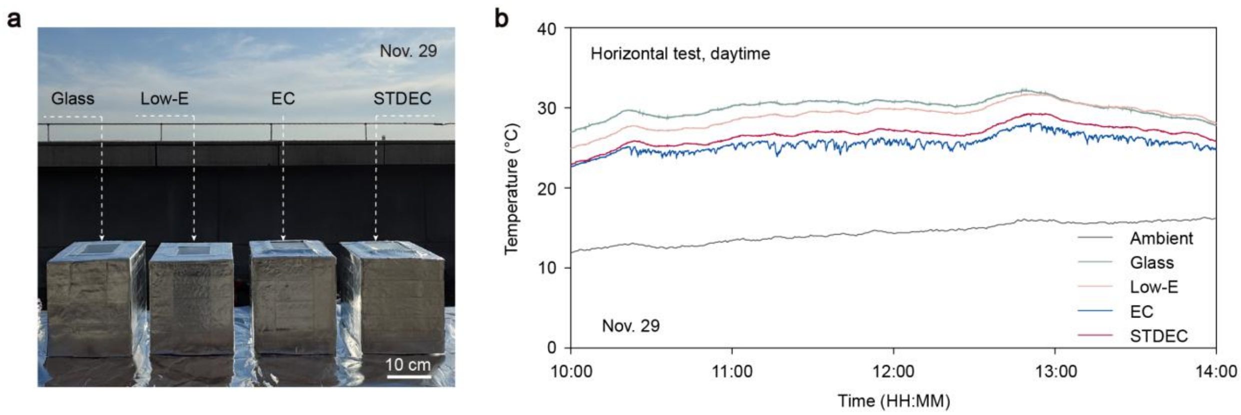

Supplementary Fig. 38: Outdoor thermal performance of the STDEC window and other reference samples during the daytime in winter. **a**, Experimental setup used for the thermal measurements of the horizontally oriented clear STDEC window and other reference samples at Nanjing University, Nanjing, China (32°07′15″N, 118°57′17″E). Scale bars, 10 cm. **b**, Temperature measurements of various horizontally positioned samples and ambient air under direct sunlight. The outdoor thermal performance assessment was carried out from 10:00 to 14:00 on 29 November 2024.

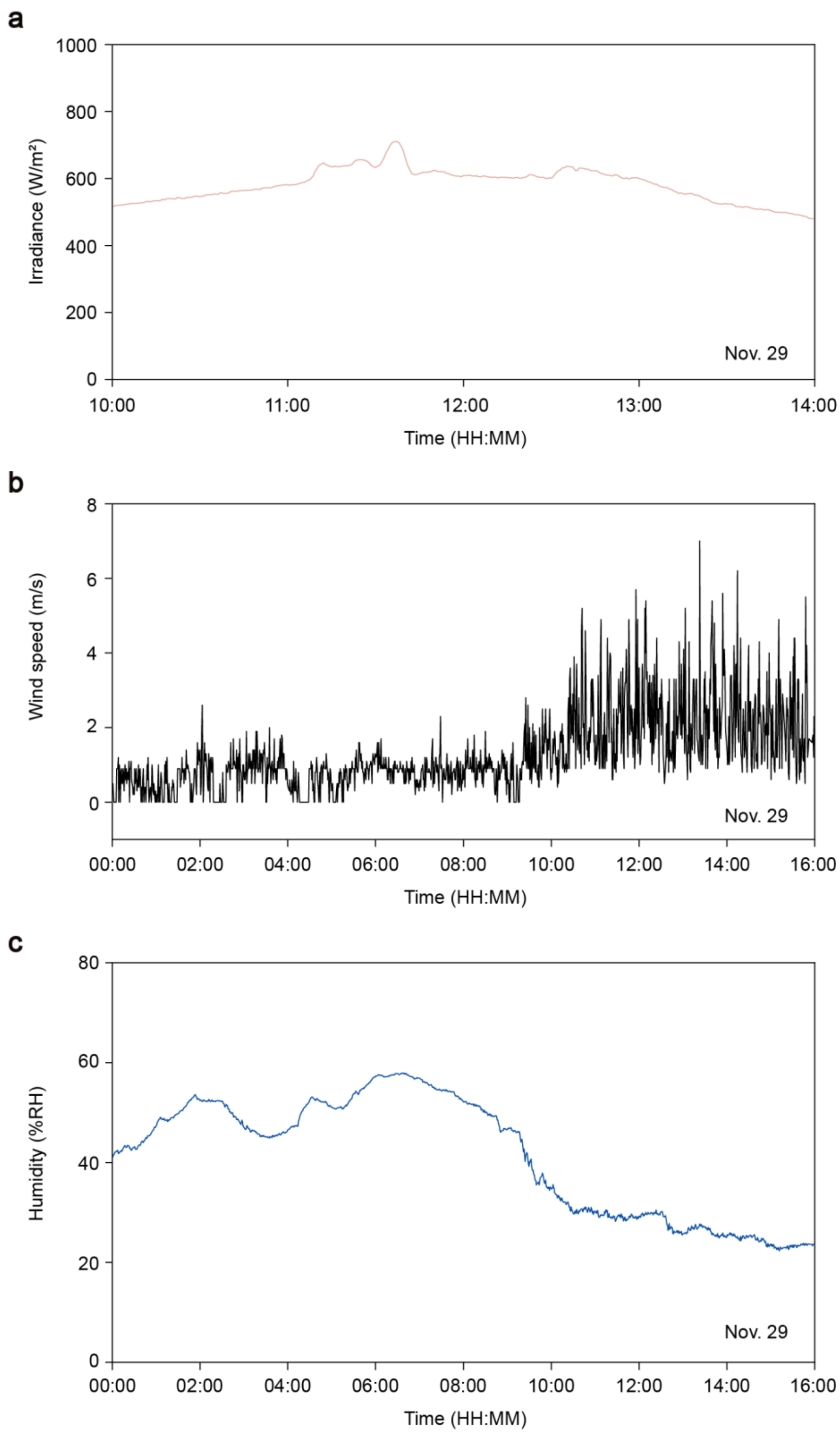

Supplementary Fig. 39: Solar irradiance, wind speed and relative humidity recorded in Nanjing on 29 November 2024.

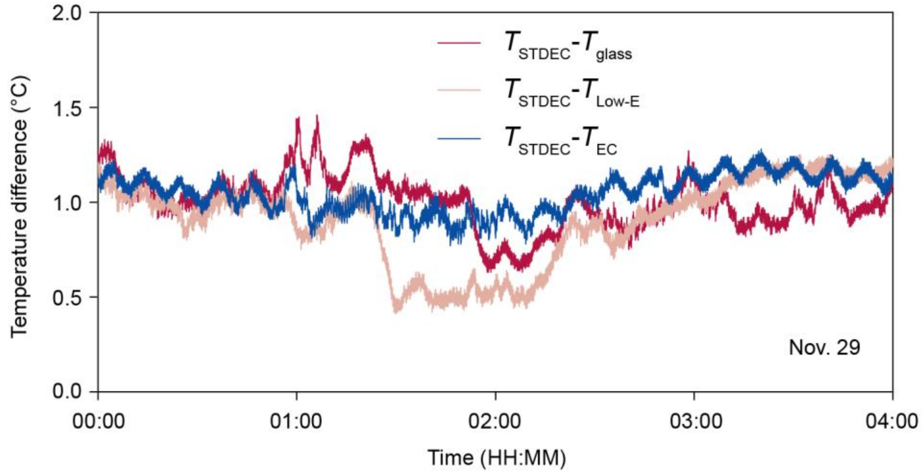

Supplementary Fig. 40: Differences in the indoor air temperatures in two different test chambers, each fitted with a specific type of window, including normal glass, low-E glass, clear RME-based EC window, and clear STDEC window, respectively.

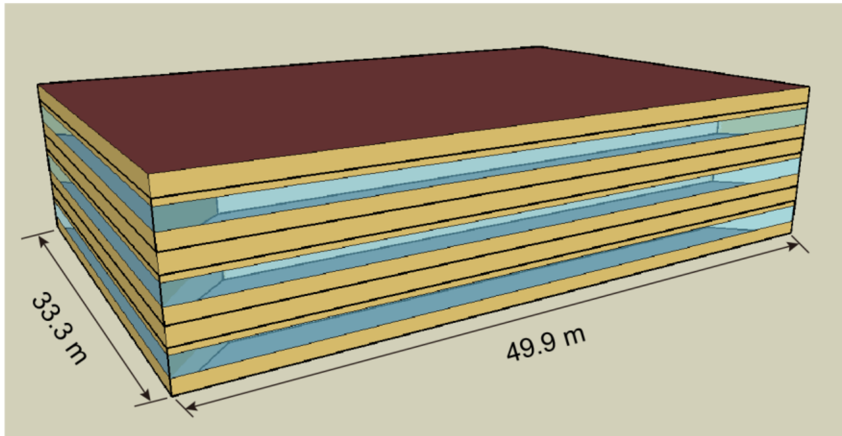

Items	Specifications
Total floor area (m²)	4982.19
Number of floors	3
Window-to-wall ratio	33%
Window locations	Even distribution among all four sides
Floor to floor height (m)	3.96
Floor to ceiling height (m)	2.74
Glazing sill height (m)	1.02

Supplementary Fig. 41: Schematic representation of the reference medium office building. The schematic is reprinted from ref.[3], CC BY 4.0 (https://creativecommons.org/licenses/by/4.0/).

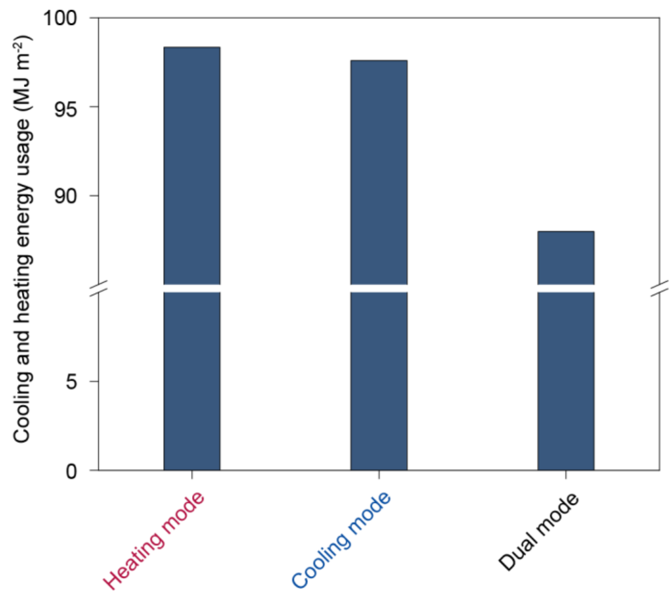

Supplementary Fig. 42: Comparison of cooling and heating energy usage using static emissivity window samples and dynamic emissivity window samples (i.e., STDEC windows). The static emissivity window samples have a constant emissivity of 0.08 (heating mode) or 0.95 (cooling mode) for heating and cooling, whereas the STDEC windows have variable emissivity values for heating and cooling, with a value of 0.08 for heating and 0.95 for cooling.

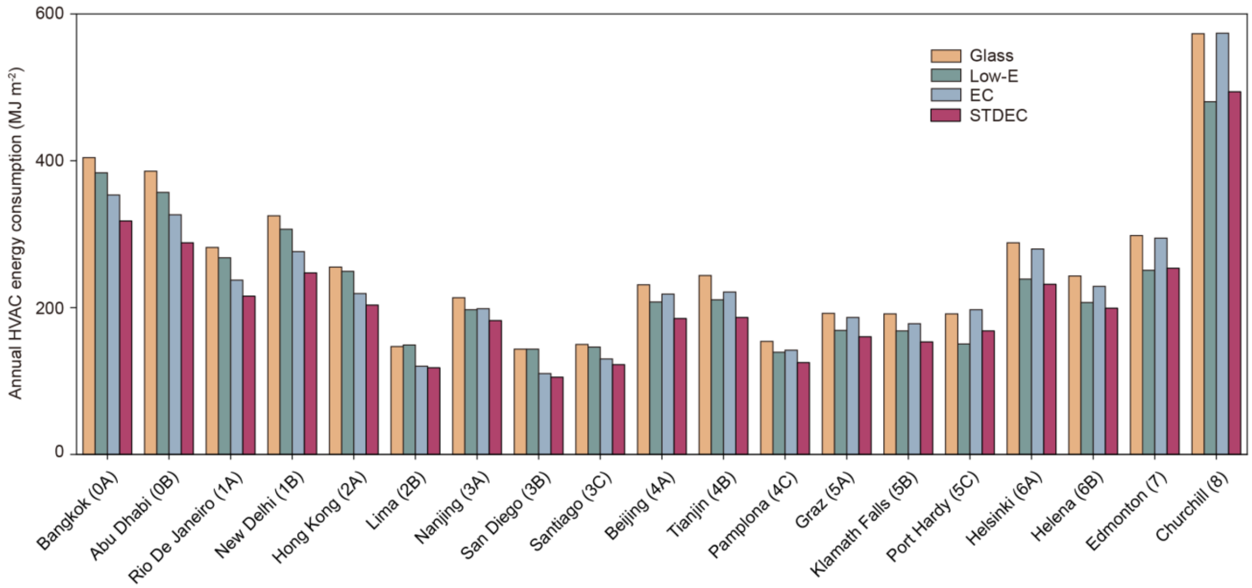

Supplementary Fig. 43: Annual HVAC energy consumption for four different window samples (i.e., normal glass, low-E glass, EC window, and STDEC window) across 19 representative cities in various climate zones.

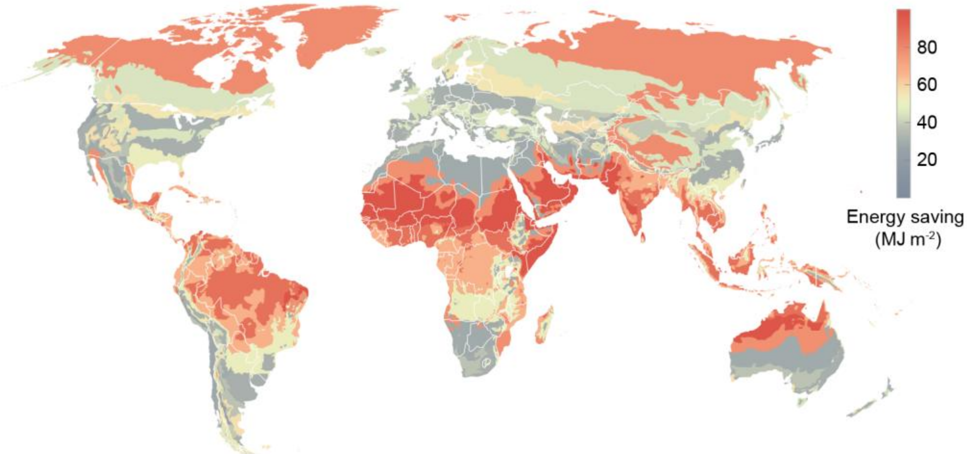

Supplementary Fig. 44: Year-round HVAC energy-saving map of the STDEC window in various global climate zones, using a normal glass as the baseline.

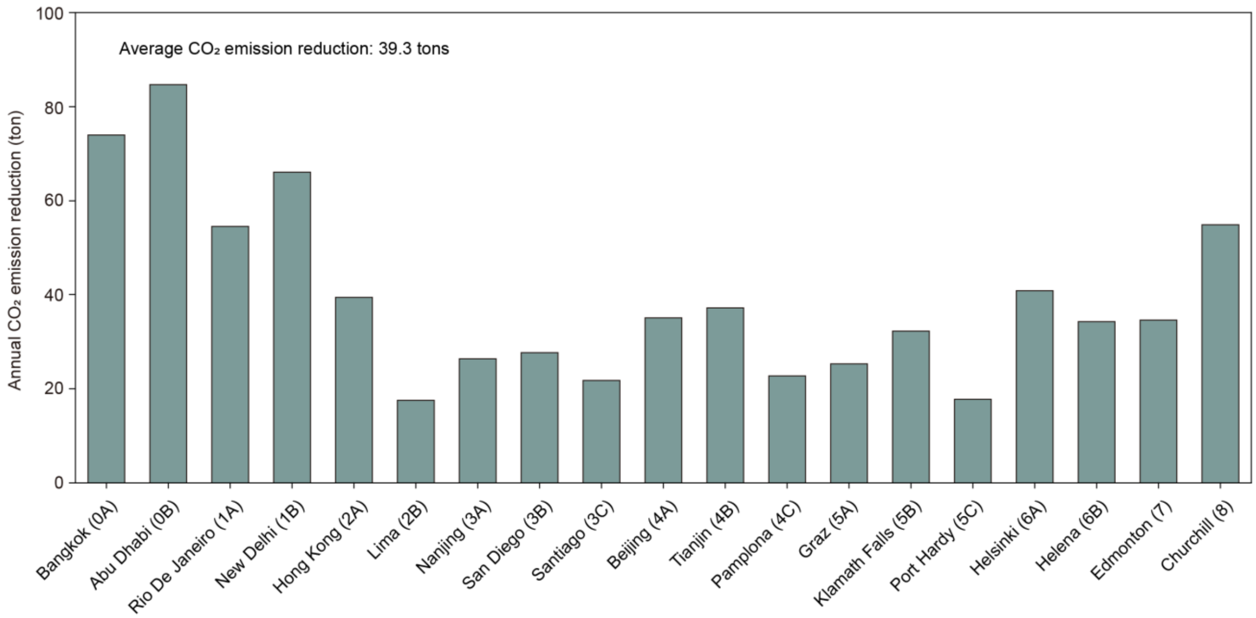

Supplementary Fig. 45: Annual CO_2 emission reductions of a medium office building with STDEC windows in 19 representative cities of different climate zones, with an average reduction of 39.3 tons compared with the normal glass baseline.

Supplementary Tables

Supplementary Table 1. Sheet resistance and optical properties of ITO with different thickness.

ITO thickness (nm)	13	65	185	260
Sheet resistance (ohm/sq)	300	30	8	5
T_{vis} (%)	80.81	81.19	80.90	59.33
T_{sol} (%)	81.48	80.86	63.39	40.65
R_{LWIR} (%)	14.25	67.16	92.12	94.10

Supplementary Table 2. Comparison of different recently reported electrochromic (EC) strategies for modulating solar transmission and thermal emissivity, corresponding to Fig. 2e.

Strategy	EC materials	Operating voltage	Cycling ability	Bistability	Color	Dual-band modulation ability	ΔT_{sol}	$\Delta \varepsilon_{LWIR}$
WO_3/VO_2[4]	WO_3/VO_2	+1.5 V for bright heating; -1.5 V for bright cooling; -3.0 V for dark	1250 (Retain 95.8%)	4 h	Clear-yellow-green-blue	No	ΔT_{sol}=44.7%	$\Delta \varepsilon_{LWIR}$=0 (Fixed high ε=0.79)
Electrodeposit Ag #1[5]	Ag	-2.5 V for deposition; +1.5 V for stripping	500	N/A	Yellow-mirror	No	ΔT_{sol}=69%	$\Delta \varepsilon_{LWIR}$=0 (Fixed high ε=0.96)
Electrodeposit Ag #2[6]	Ag	-1.5 V for deposition; +0.3 V for stripping	350 (Retain 80%)	100 s	Mirror-black	No	ΔT_{sol}=0 (Opaque)	$\Delta \varepsilon_{(2.5-18\ \mu m)}$=0.74
Electrodeposit Cu[7]	Cu	-0.7 V for deposition; +1.0 V for stripping	1800 (Retain 79%)	5.5 h	Mirror	No	ΔT_{sol}=0 (Opaque)	$\Delta \varepsilon_{(7.5-13\ \mu m)}$=0.85
Graphene[8]	Multilayer graphene	0 V for Li^+ extraction; 3.8 V for Li^+ insertion	2200 (Retain 85%)	N/A	Black-gold	No	ΔT_{sol}=0 (Opaque)	$\Delta \varepsilon_{(10\ \mu m)}$=0.45
AZO[9]	AZO	-2.5 V for electron injection; +2.5 V for electron extraction	10,000 (Retain 83.4%)	1351 s; 1.29 s	Clear	No	ΔT_{sol}=0 (Transparent)	$\Delta \varepsilon_{(7.5-13\ \mu m)}$=0.41
Liquid crystal[10]	E7 nematic liquid crystal	0 V for white opacity; 60 V for transparency	200	N/A	Clear-white opacity	Yes	ΔT_{sol}=42.4%	$\Delta \varepsilon_{(2.5-14\ \mu m)}$=0.65
Polyaniline[11]	Polyaniline	-1.0 V for yellow; +0.4 V for green; +1.0 V for blue	6000 (Retain 82%)	N/A	Yellow-green-blue	Yes	ΔT_{sol}=43.5%	$\Delta \varepsilon_{(8-13\ \mu m)}$=0.74
This work	**Cu–Bi**	**-1.0 V for deposition; +1.0 V for stripping**	**2000 (Retain ~100%)**	**36 h**	**Clear-grey-black**	**Yes**	**ΔT_{sol}=52.2%**	**$\Delta \varepsilon_{(2.5-20\ \mu m)}$=0.87**

Supplementary Table 3. Haze calculation of the STDEC window.

STDEC sample	τ_1 (%)	τ_2 (%)	τ_3 (%)	τ_4 (%)	Haze (%)
Stripping state	100	55.90	0	0.24	0.43
Depositing state	100	8.53	0	0.07	0.82

Note: To quantitatively assess the optical clarity of the window, we calculated the Haze in both the stripping and depositing states using the following formula:

$$\text{Haze (\%)} = \left[\left(\frac{\tau_4}{\tau_2}\right) - \tau_3\left(\frac{\tau_2}{\tau_1}\right)\right] \times 100 \quad (1)$$

where τ_1 is the total transmittance without the sample (100%); τ_2 is the total transmittance with the sample; τ_3 is the diffuse transmittance without the sample; and τ_4 is the diffuse transmittance with the sample. Supplementary Figure 25 presents the total and diffuse transmittance spectra of the STDEC window in the stripping and depositing states, along with the diffuse transmittance spectrum measured without the window sample. All spectra were obtained using an integrating sphere. There is nearly no diffuse transmittance across the solar spectrum, which explains the low measured haze values (Haze = 0.43% at T_{sol} = 55.90%; Haze = 0.82% at T_{sol} = 8.53%; Supplementary Table 3) and demonstrates the excellent optical clarity of the STDEC windows.

Supplementary Table 4. $L^*a^*b^*$ and chroma (C^*) measurements of a STDEC window at various depositing times.

Depositing time (s)	L^*	a^*	b^*	C^*
0	91.7	0.4	-1.0	1.1
5	73.7	-1.8	1.7	2.5
10	63.3	-1.7	3.5	3.9
30	32.2	-3.3	5.5	6.4
50	12.1	-0.7	2.0	2.1

Supplementary Table 5. $L^*a^*b^*$ and chroma (C^*) measurements of a STDEC window at various stripping times.

Stripping time (s)	L^*	a^*	b^*	C^*
0	12.1	-0.7	2.0	2.1
5	24.5	-2.2	3.4	4.0
10	45.7	-0.7	7.3	7.3
15	62.8	-3.0	8.4	8.9
20	90.4	0.7	0.2	0.7

Note: L^* quantifies lightness on a scale from 0 (black) to 100 (white), a^* indicates the green to red ranging from -128 (pure green) to +128 (pure red), and b^* measures the blue to yellow ranging from -128 (pure blue) to +128 (pure yellow). C^* is a metric that combines a^* and b^* values in the color space to characterize the overall color of the STDEC window. When C^* is less than 10, it becomes challenging for the human eye to differentiate the color of the window, leading to a perception of color neutrality. In these instances, the C^* value falls below 10 for STDEC window, resulting in a color-neutral appearance.

Supplementary Table 6. Optical and thermal properties for window samples used in building energy simulation.

Optical properties	Normal glass	Low-E glass	EC window (heating mode)	EC window (cooling mode)	STDEC window (heating mode)	STDEC window (cooling mode)
T_{vis} (%)	88.1	85.0	67.2	0.04	64.8	0.04
$R_{vis\text{-}Front}$ (%)	8.0	5.6	11.2	10.3	15.0	16.0
$R_{vis\text{-}Back}$ (%)	8.0	7.9	10.8	25.5	14.9	16.5
T_{sol} (%)	77.5	63.0	53.3	0.06	52.2	0.06
$R_{sol\text{-}Front}$ (%)	7.1	19.0	9.6	8.2	17.8	15.7
$R_{sol\text{-}Back}$ (%)	7.1	22.0	16.5	33.8	11.4	20.2
$\varepsilon_{LWIR\text{-}Front}$	0.84	0.84	0.84	0.84	0.08	0.95
$\varepsilon_{LWIR\text{-}Back}$	0.84	0.1	0.84	0.84	0.95	0.08
U-value (W m^{-2} K^{-1})	5.8	5.7	5.5	5.5	4.6	3.2
SHGC	0.89	0.76	0.79	0.69	0.69	0.40

Supplementary Table 7. Annual CO_2 emission reductions of a medium office building with STDEC windows in 19 representative cities of different climate zones.

Region	Thermal zone	Thermal climate zone name	Annual CO_2 emission reduction (ton)
Bangkok, Thailand	0A	Extremely Hot Humid	74.0
Abu Dhabi, United Arab Emirates	0B	Extremely Hot Dry	84.7
Rio De Janeiro, Brazil	1A	Very Hot Humid	54.5
New Delhi, India	1B	Very Hot Dry	66.1
Hong Kong, China	2A	Hot Humid	39.4
Lima, Peru	2B	Hot Dry	17.5
Nanjing, China	3A	Warm Humid	26.4
San Diego, USA	3B	Warm Dry	27.7
Santiago, Chile	3C	Warm Marine	21.8
Beijing, China	4A	Mixed Humid	35.1
Tianjin, China	4B	Mixed Dry	37.2
Pamplona, Spain	4C	Mixed Marine	22.7
Graz, Austria	5A	Cool Humid	25.3
Klamath Falls, USA	5B	Cool Dry	32.3
Port Hardy, Canada	5C	Cool Marine	17.8
Helsinki, Finland	6A	Cold Humid	40.9
Helena, USA,	6B	Cold Dry	34.3
Edmonton, Canada	7	Very Cold	34.6
Churchill, Canada	8	Subarctic/Arctic	54.9

Supplementary Note 1. Heat transfer analysis of the single-glazed window.

In this section, we aim to analyze how solar and thermal radiation affect heat transfer across traditional single-glazed windows, which will guide the creation of the STDEC smart window. The total heat transfer through a window includes conductive, radiative and convective components caused by a temperature difference. In general, heat transfer through conduction, long-wave radiation, and convection is associated with the overall heat transfer coefficient (*U*-value) of the window. Additionally, short-wave solar radiation largely contributes to the heat flows, and is related to the solar heat gain coefficient (SHGC) of the window. To simplify our analysis, we ignored the effects of convection. The total heat transfer (Q_{tot}) of the single-glazed window is broken down into components:

$$Q_{\text{tot}} = Q_{\text{cond}} + Q_{\text{sw}} + Q_{\text{lw}} \tag{2}$$

where, Q_{cond}, Q_{sw}, and Q_{lw} are the conductive heat transfer, short-wave solar radiation heat gain, and long-wave thermal radiation heat loss, respectively. Q_{cond} can be quantified by:

$$Q_{\text{cond}} = U \cdot A \cdot \Delta T \cdot t \tag{3}$$

where U is the heat transfer coefficient (W/(m^2·K)), A is the window area (m^2), ΔT is the indoor-outdoor temperature difference (K), and t is the time duration (hours). Q_{sw} can be simply calculated as follows:

$$Q_{\text{sw}} = \text{SHGC} \cdot A \cdot I_{\text{sol}} \cdot t \tag{4}$$

where SHGC is the solar heat gain coefficient, and I_{sol} is the solar irradiance (W/m^2). Q_{lw} can be expressed as follows[12]:

$$Q_{\text{lw}} = \varepsilon_{\text{lw}} \cdot \sigma \cdot A \cdot \left(T_{\text{window}}^4 - T_{\text{sky}}^4\right) \cdot t \tag{5}$$

where ε_{lw} and σ are the emissivity of the window surface and Stefan-Boltzmann constant, 5.67×10^{-8} W/(m^2·K^4), respectively. T_{window} is the window surface temperature (K), and T_{sky} is the effective sky temperature (K), as given by[12,13]:

$$T_{\text{sky}} = \left(\varepsilon_{\text{sky}} T_a^4\right)^{\frac{1}{4}} \tag{6}$$

where ε_{sky} is the sky emissivity, which is usually adopted as 0.8, and T_a is the ambient temperature.

To accurately determine the contribution of solar and thermal radiation in the total heat transfer from the window, we conducted seasonal case studies. In hot summer, the calculated parameters of the single-glazed window are described as follows:

A = 10 m^2; U-value = 5.8 W/(m^2·K); SHGC = 0.8; ε_{lw} = 0.84; indoor air temperature is 25°C, outdoor air (ambient) temperature is 30°C, ΔT = 5 K, and I_{sol} = 500 W/m^2 (12 hours for daytime), as specified by ISO 15099 (2003)[14,15]; T_{window} = 313 K (daytime)[16], T_{window} = 298 K (nighttime); and T_{sky} = 287 K. Using these criteria, we determined the Q_{cond}, Q_{sw}, Q_{lw} and Q_{tot} values from the window accordingly:

$$Q_{\text{cond}} = 5.8 \times 10 \times 5 \times 24 = 7.0 \text{ kWh} \tag{7}$$

$$Q_{\text{sw}} = 0.8 \times 10 \times 500 \times 12 = 48 \text{ kWh} \tag{8}$$

$$Q_{\text{lw, day}} = 0.84 \times 5.67 \times 10^{-8} \times 10 \times (313^4 - 287^4) \times 12 = 16.1 \text{ kWh} \tag{9}$$

$$Q_{\text{lw, night}} = 0.84 \times 5.67 \times 10^{-8} \times 10 \times (298^4 - 287^4) \times 12 = 6.3 \text{ kWh} \tag{10}$$

$$Q_{\text{tot}} = Q_{\text{cond}} + Q_{\text{sw}} + \left(Q_{\text{lw, day}} + Q_{\text{sw, night}}\right) = 77.4 \text{ kWh} \tag{11}$$

Ultimately, we calculated the contribution ratios of conductive heat gain, solar radiation gain, and thermal radiation loss to the total heat transfer in hot summer. Note that solar radiation accounts for more than 60% of the total heat transfer in these conditions. For more detailed results, please refer to Supplementary Table 8.

In cold winter, the calculated parameters of the single-glazed window are described as follows: A = 10 m^2; U-value = 5.8 W/(m^2·K); SHGC = 0.8; ε_{lw} = 0.84; indoor air temperature is 20°C, outdoor air (ambient) temperature is 0°C, ΔT = 20 K, and I_{sol} = 300 W/m^2 (6 hours for daytime), as specified by ISO 15099 (2003)[14,15]; T_{window} = 293 K; and T_{sky} = 258 K. According to these parameters, we calculated the Q_{cond}, Q_{sw}, Q_{lw} and Q_{tot} values from the window, respectively:

$$Q_{\text{cond}} = 5.8 \times 10 \times 20 \times 24 = 27.8 \text{ kWh} \tag{12}$$

$$Q_{\text{sw}} = 0.8 \times 10 \times 300 \times 6 = 14.4 \text{ kWh} \tag{13}$$

$$Q_{\text{lw}} = 0.84 \times 5.67 \times 10^{-8} \times 10 \times (293^4 - 258^4) \times 24 = 33.6 \text{ kWh} \tag{14}$$

$$Q_{\text{tot}} = Q_{\text{cond}} + Q_{\text{sw}} + Q_{\text{lw}} = 75.8 \text{ kWh} \tag{15}$$

Finally, we quantified the contribution ratios of conductive heat loss, solar radiation gain, and thermal radiation loss to the total heat transfer in cold winter. Notably, thermal radiation contributes over 40% of the total heat transfer in these conditions. A more detailed outcome can be found in Supplementary Table 8.

In conclusion, properly managing solar radiation and thermal radiation through windows could reduce the year-round energy consumption in buildings, while enhancing energy efficiency. In the summer, it's crucial to reduce the solar radiation entering through windows and further improve their ability to emit thermal radiation to cool down buildings. On the other hand, in the winter, we should aim to maximize solar radiation transmission and minimize thermal emissivity to warm up buildings.

Supplementary Table 8. The contribution percentages of conductive heat transfer (Q_{cond}), solar radiation gain (Q_{sw}), and thermal radiation loss (Q_{lw}) to the total heat transfer (Q_{tot}).

Season	Q_{cond}/Q_{tot}	Q_{sw}/Q_{tot}	Q_{lw}/Q_{tot}
Summer	9.0% (heat gain)	62.0% (heat gain)	29.0% (heat loss)
Winter	36.7% (heat loss)	19.0% (heat gain)	44.3% (heat loss)

Supplementary Note 2. Formation and removal mechanism of the Cu–Bi film.

This section elucidates the formation and removal mechanism of the Cu–Bi film under applied bias and cycling conditions. Supplementary Figure 46 shows the cyclic voltammetry (CV) curve for the deposition and stripping of the Cu–Bi film, obtained within a voltage range of –1.0 V to +1.0 V at 50 mV/s. During the initial negative-going sweep, the cathodic current starts to rise at 0.52 V, attributed to the reduction of Cu^{2+} to Cu^{+} without any metal deposition. A further increase in cathodic current at –0.2 V, corresponds to the reduction of Bi^{3+} to Bi and Cu^{+} to Cu. At this phase, Cu^{+} can participate in galvanic displacement reactions with dendritic Bi atoms and fill in void spaces with three times the number of Cu atoms, resulting in a more condensed spherical morphology that suppresses dendritic growth (Supplementary Fig. 47).

During the subsequent positive-going sweep, the negative current indicates the continued reduction of metal ions to Cu–Bi films deposited on the working electrode. Anodic current begins to increase at –0.1 V, due to the dissolution of the Cu and Bi back to Cu^{+} and Bi^{3+}, respectively. At this stage, Cu^{+} can also speed up the dissolution of Bi via galvanic displacement reactions, leaving no residual dead Bi (Supplementary Fig. 47). Cu^{+} is then further oxidized to Cu^{2+} at voltages more positive than 0.65 V.

These deposition and stripping processes can be linked to the current–time curve (Supplementary Fig. 24). When a negative voltage (–1.0 V) is applied, the current–time curve exhibits a transient current peak (Supplementary Fig. 24, i), indicating the instantaneous nucleation of Cu–Bi clusters on the electrode surface. After this peak, the current slowly decays and reaches a diffusion-controlled plateau phase (Supplementary Fig. 24, ii), reflecting the concurrent nucleation and growth of the Cu–Bi film. When the bias is reversed to +1.0 V, a reverse anodic current peak appears (Supplementary Fig. 24, iii) and then gradually diminishes (Supplementary Fig. 24, iv), which corresponds to the stripping and dissolution of the Cu–Bi film. These symmetric peaks, with a charge of about 100.5 mC/cm^2, indicate excellent electrochemical reversibility and stable cycling performance of the Cu–Bi film.

Cu^{2+} critically governs the deposition and stripping of Cu–Bi films, determining switching speed, reversibility, and cycling stability. Upon deposition, Cu^{2+} is reduced to Cu^{+}, which drives galvanic displacement of Bi and promotes the nucleation and growth of spherical particles. Upon stripping, Cu is oxidized to Cu^{+}, and the same displacement mechanism, aided by the spherical morphology, enables fast and clean Bi dissolution. Together, these effects result in excellent switching speed, reversibility, and cycling stability achieved in our work.

In contrast, a Bi-based RME device with the Bi-only electrolyte exhibits poor switching speed, reversibility, and cycling stability (Supplementary Fig. 48). Even after 120 s of deposition, the device still has a solar transmittance (T_{sol}) of over 5% (Supplementary Fig. 48a), indicating slow switching speed. After only 10 cycles, non-uniform deposition and incomplete stripping are observed (Supplementary Fig. 48b), reflecting poor reversibility arising from the dendritic growth morphology of pure Bi deposits (Supplementary Fig. 48c). This is further supported by a charge imbalance between deposition and stripping in the chronoamperometric curve (Supplementary Fig. 48d). As a result, the device retains only 22.5% of its initial contrast after 50 cycles (Supplementary Fig. 48e), demonstrating extremely limited cycling stability.

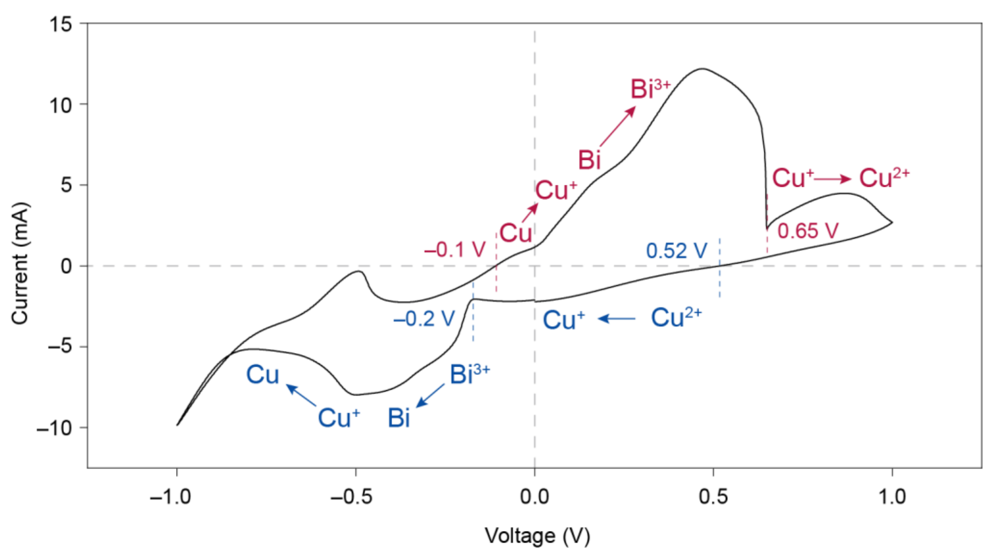

Supplementary Fig. 46: Cyclic voltammogram of the Cu–Bi film measured between –1.0 V and +1.0 V at 50 mV/s.

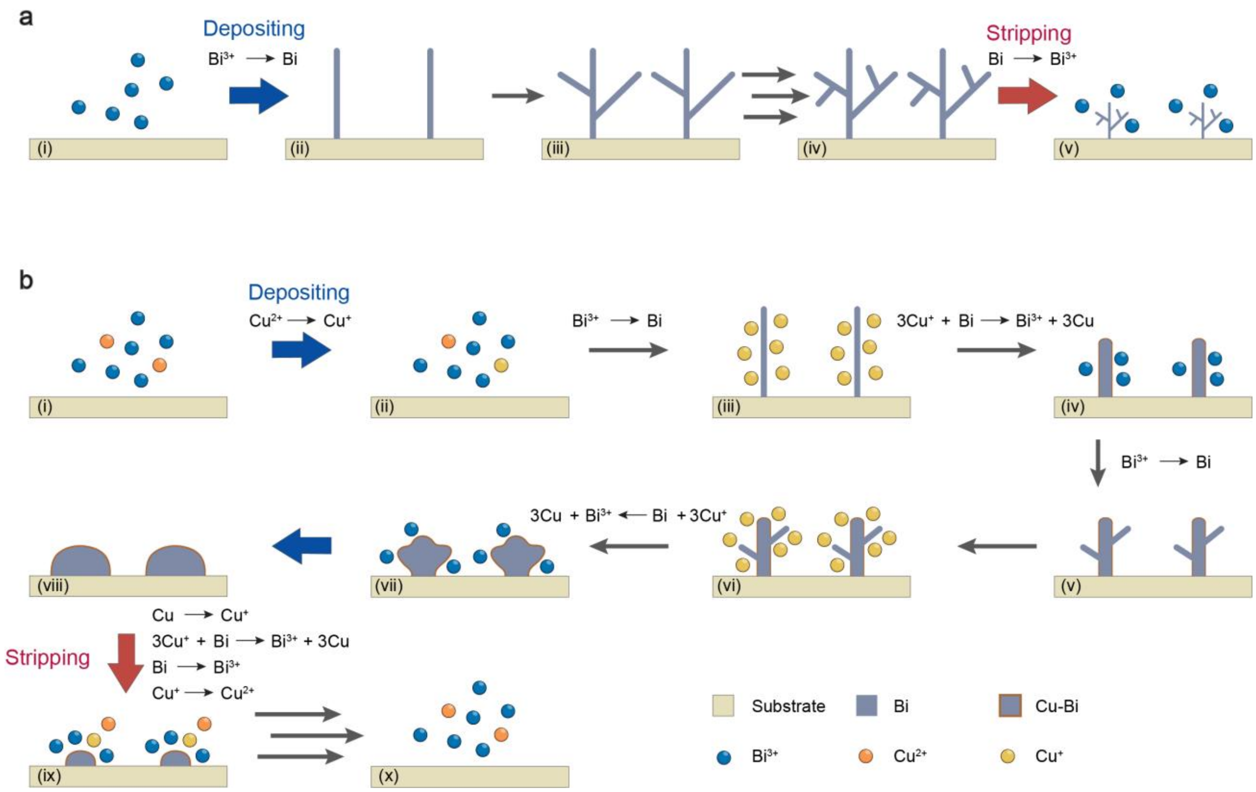

Supplementary Fig. 47: Reaction schematic for the deposition and stripping of Bi films in the (**a**) absence and (**b**) presence of Cu^{2+}.

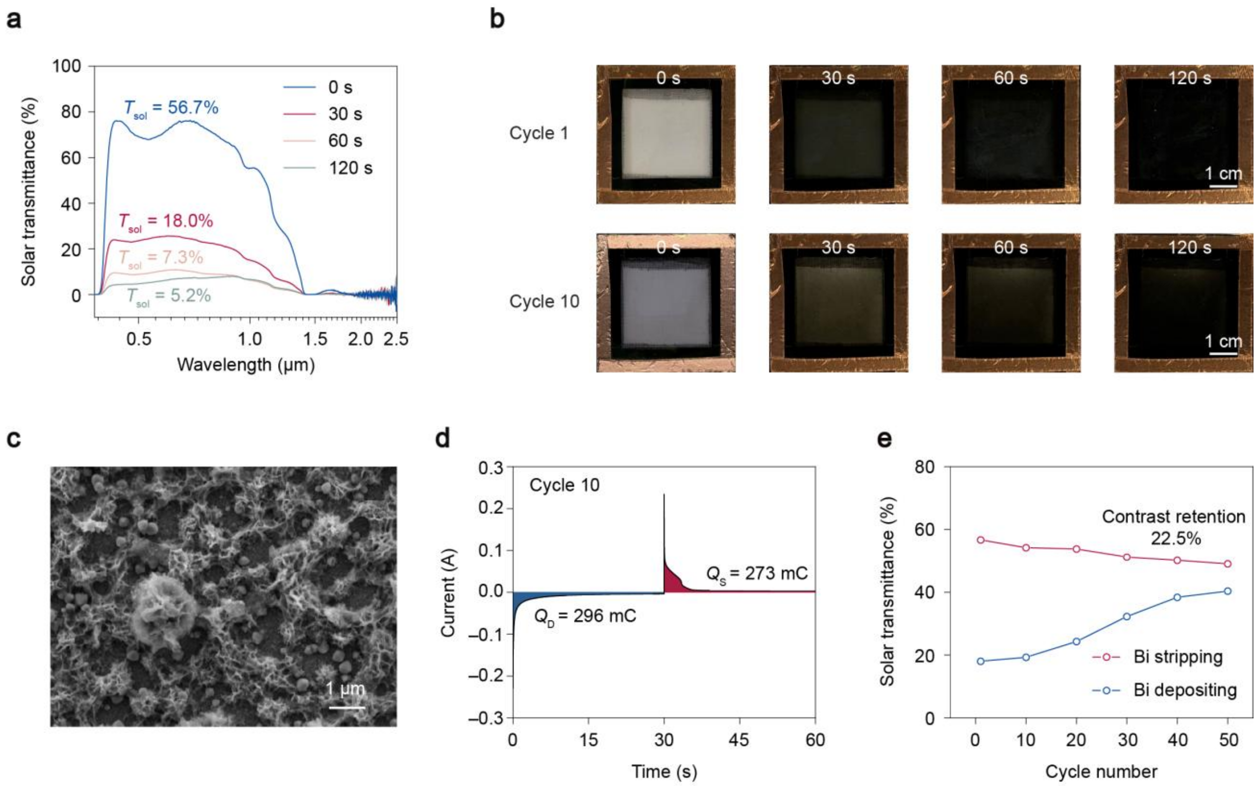

Supplementary Fig. 48: Electrochromic performance of a Bi-based RME device using the Bi-only electrolyte. **a**, Solar transmittance spectra recorded at different depositing times. **b**, Optical photographs of the device at cycle 1 and 10 for various depositing times. **c,** SEM images of the deposited Bi films at cycle 10, revealing a dendritic morphology. **d**, Chronoamperometric curve exhibiting the charge imbalance between deposition and stripping. **e**, Cycling performance of the deices across the solar spectrum.

Supplementary Note 3. Calculation of the yearly electrical energy usage for switching the STDEC window.

To determine the yearly electrical energy usage for operating the STDEC window, we first computed the average power consumption of the STDEC window, as illustrated in Supplementary Fig. 24:

$$\overline{P} = 3.35\ \mathrm{mW/cm^2} \tag{16}$$

The STDEC window is capable of effectively blocking light and heat after 60 s of depositing Cu–Bi films, resulting in T_{vis} and T_{sol} below 1.0%. According to the deposition time, we proceeded to calculate the average electricity usage per unit area (E_{device}) of the STDEC window:

$$E_{\mathrm{device}} = \overline{P}t = (3.35 \times 10) \times 60 = 2010\ (\mathrm{J/m^2}) \tag{17}$$

To calculate the total electricity consumption in a three-floor medium office (Supplementary Fig. 41), begin by multiplying the E_{device} by the total window areas (652.62 $\mathrm{m^2}$). We then calculated the average electricity usage per unit floor (E_{unit}) by dividing the total electricity consumption by the number of floors (3 stories) and the area of each floor. This can be represented by the following equation:

$$E_{\mathrm{unit}} = \frac{E_{\mathrm{device}} \times S_{\mathrm{window}}}{3\ \mathrm{stories} \times S_{\mathrm{floor}}} = \frac{2010 \times 652.62}{4982.19} = 263.29\ (\mathrm{J/m^2}) \tag{18}$$

Finally, we determined the yearly electrical energy usage (E_{yearly}) for operating the STDEC window even with a conservative assumption of the windows being switched five times a day.

$$E_{\mathrm{yearly}} = 365 \times 5 \times E_{\mathrm{unit}} = 480{,}504.25\ (\mathrm{J/m^2}) \approx 0.48\ (\mathrm{MJ/m^2}) \tag{19}$$

It is important to mention that the annual electrical energy usage (0.12 to 0.96 $\mathrm{MJ/m^2}$) required to attain different time-dependent optical states (as shown in Supplementary Fig. 14) can also be calculated using the previously described method.

Supplementary Note 4. Techno-economic assessment (TEA) analysis of the STDEC window.

To assess the energy-saving performance of the STDEC window for real-world applications, we conducted a comprehensive techno-economic assessment (TEA) accounting for manufacturing costs, service life, or maintenance costs.

(i) Cost analysis of the whole device

As summarized in Supplementary Tables 9–11, the manufacturing cost of the STDEC window is about $6.38 per square meter of window area. Based on our building simulation model with a total window area of 652.62 m^2 and a total building area of 4982.19 m^2, this equates to approximately $0.84 per square meter of building area.

To contextualize this cost in terms of energy consumption, we converted it into an equivalent energy metric based on the electricity cost of $0.1745 per kWh, as reported by the U.S. Energy Information Administration (EIA). This manufacturing cost corresponds to an energy equivalent of 17.33 MJ m^{-2} of building area.

Supplementary Table 9. Cost analysis of electrolyte components.

Chemical's name	Price (US $/gram)
PVA	0.0022
$CuCl_2$	0.006
$BiCl_3$	0.0017
HCl	0.0011
LiBr	0.0014
Water	0.00084

Supplementary Table 10. Cost analysis of device materials.

Material	Price (US $)
Glass	1.50/m^2 (Alibaba)
ITO	1.02/gram (Qinbangxc)
Cu mesh	3.76/m^2 (TWP)
PE	0.057/m^2 (Amazon)
3-nm-thick Pt	0.12/m^2 (Alibaba)
Butyl rubber tape	0.0047/gram (Alibaba)

Supplementary Table 11. Cost analysis of the whole device.

Component	Price (US $/$m^2$)
Electrolyte	1.9
Cu mesh	0.15
ITO/Glass/ITO	4.07
3-nm-thick Pt	0.12
PE	0.057
Butyl rubber tape	0.086
Device	**6.38**

(ii) Service life

As reported in our work, the STDEC window demonstrates excellent cycling stability over 2,000 cycles, with only 1% degradation in optical contrast. At a typical operational frequency of two switching cycles per day for smart windows, this corresponds to approximately 2.7 years of service. If we then assume a steady degradation rate of 1% per year, the optical contrast would decline to 80% of its initial value after another 19 years, which we conservatively define as the end of lifetime. Therefore, the total estimated service life is ~21.7 years, which exceeds the 20-year service life for commercial smart windows.

The manufacturing cost (equivalent to 17.33 MJ/m^2 of building area), when amortized over the service life, corresponds to an annualized energy equivalent of only about 0.80 MJ m^{-2} yr^{-1}.

(iii) Maintenance cost

The maintenance cost is dominated by the electricity consumption during switching. As reported in our work, the average electricity usage per square meter of building area of the STDEC window is 263.29 J m^{-2}. At a typical operational frequency of two switching cycles per day, the yearly electrical energy usage is about 0.19 MJ m^{-2} yr^{-1}.

In summary, the total annualized energy usage accounting for manufacturing costs, service life, and maintenance costs of the STDEC window is calculated to 0.99 MJ m^{-2} yr^{-1}. This value is nearly two orders of magnitude lower than the simulated annual HVAC energy savings (up to 80 MJ m^{-2} yr^{-1}), confirming the excellent energy-efficient performance of the STDEC window.

Supplementary Note 5. Calculation of SHGC and *U*-value for the windows.

The solar heat gain coefficient (SHGC) is defined as:

$$\mathrm{SHGC} = \left(T_{\mathrm{sol}} + \frac{U}{h_{\mathrm{o}}} A_{\mathrm{sol}}\right) \tag{20}$$

where T_{sol} is the solar transmittance;

A_{sol} is the solar absorbance;

h_o is the outdoor surface heat transfer coefficient, $h_o = 8.0$ W m^{-2} K^{-1} (refer to ISO-15099-2003)[15];

U is the universal heat transfer coefficient, which can be given by:

$$U = \frac{1}{\frac{1}{h_{\mathrm{conv,o}}+h_{\mathrm{rad,o}}} + \frac{1}{h_{\mathrm{conv,i}}+h_{\mathrm{rad,i}}} + \frac{L_{\mathrm{device}}}{k_{\mathrm{device}}}} \tag{21}$$

where $h_{conv,\,o}$ is the outdoor convective heat transfer coefficient, $h_{conv,\,o} = 8.0$ W m^{-2} K^{-1};

$h_{conv,\,i}$ is the indoor convective heat transfer coefficient, $h_{conv,\,i} = 3.6$ W m^{-2} K^{-1};

$h_{rad,\,o}$ is the outdoor radiative heat transfer coefficient;

$h_{rad,\,i}$ is the indoor radiative heat transfer coefficient;

k_{device} and L_{device} are the thermal conductivity and thickness of the window device.

The outdoor convective heat transfer coefficient ($h_{rad,\,o}$) can be calculated as:

$$h_{\mathrm{rad,o}} = \frac{\varepsilon_{\mathrm{device,o}}\sigma\left(T_{\mathrm{device,o}}^4 - T_{\mathrm{rm,o}}^4\right)}{T_{\mathrm{device,o}} - T_{\mathrm{rm,o}}} = \varepsilon_{\mathrm{device,o}}\sigma\left(T_{\mathrm{device,o}}^2 + T_{\mathrm{rm,o}}^2\right)\left(T_{\mathrm{device,o}} + T_{\mathrm{rm,o}}\right) \tag{22}$$

where $\varepsilon_{device,\,o}$ is the emissivity of the outside device surface;

σ is Stefan-Boltzmann constant, 5.67×10^{-8} W m^{-2} K^{-4};

$T_{device,\,o}$ is the temperature of the outside device surface;

$T_{rm,\,o}$ is the mean radiative temperature of outside ambient, which can be expressed as:

$$T_{\mathrm{rm,o}} = \left(\frac{\left(F_{\mathrm{gd}} + (1 - f_{\mathrm{clr}})F_{\mathrm{sky}}\right)\sigma T_{\mathrm{ex}}^4 + f_{\mathrm{clr}} F_{\mathrm{sky}} J_{\mathrm{sky}}}{\sigma}\right)^{\frac{1}{4}} \tag{23}$$

$$F_{\mathrm{gd}} = 1 - F_{\mathrm{sky}} \tag{24}$$

$$F_{\mathrm{sky}} = \frac{1 + \cos\phi}{2} \tag{25}$$

$$J_{\mathrm{sky}} = 5.31 \times 10^{-13} T_{\mathrm{air}}^6 \tag{26}$$

where F_{gd} and F_{sky} are the view factors from the outside glass surface to the ground and sky, respectively;

f_{clr} is the fraction of the sky that is clear;

T_{ex} is the external air temperature;

Φ is the tilt angle of the glass;

J_{sky} is the radiosity of clear sky;

T_{air} is the dry bulb temperature.

For a horizontal window ($F_{\text{sky}} = 1, F_{\text{gd}} = 0, f_{\text{clr}} = 1$):

$$T_{\text{rm,o}} = \left(\frac{J_{\text{sky}}}{\sigma}\right)^{\frac{1}{4}} \quad (27)$$

The indoor radiative heat transfer coefficient ($h_{\text{rad, i}}$) can be determined by:

$$h_{\text{rad,i}} = \frac{\varepsilon_{\text{device,i}}\sigma\left(T_{\text{device,i}}^4 - T_{\text{rm,i}}^4\right)}{T_{\text{device,i}} - T_{\text{rm,i}}} = \frac{\varepsilon_{\text{device,i}}\sigma\left(T_{\text{device,i}}^4 - T_{\text{int}}^4\right)}{T_{\text{device,i}} - T_{\text{int}}} = \varepsilon_{\text{device,i}}\sigma\left(T_{\text{device,i}}^2 + T_{\text{int}}^2\right)\left(T_{\text{device,i}} + T_{\text{int}}\right) \quad (28)$$

where $\varepsilon_{\text{device, i}}$ is the emissivity of the inside device surface;

σ is Stefan-Boltzmann constant, 5.67×10^{-8} W m^{-2} K^{-4};

$T_{\text{device, i}}$ is the temperature of the inside device surface;

$T_{\text{rm, i}} = T_{\text{int}}$ is the internal air temperature.

Supplementary Table 12 presents the temperatures recorded from outdoor thermal measurements required for the calculation. Based on these data and the optical properties of the windows (Supplementary Table 6), we calculated the *U*-values and SHGC for the STDEC window and the control windows (normal glass, low-E glass, and EC window). Among all the windows tested, the STDEC window has the lowest *U*-value and the largest dynamic SHGC modulation range between the heating and cooling modes, highlighting its excellent optical and thermal regulation capability.

Supplementary Table 12. Outdoor temperature measurement conducted at a dry bulb temperature of T_{air} = 298 K.

Temperature (K)	EC window (heating mode)	EC window (cooling mode)	STDEC window (heating mode)	STDEC window (cooling mode)
Outside surface ($T_{device, o}$)	315	319	316	318
Inside surface ($T_{device, i}$)	320	323	320	319
Internal air (T_{int})	325	314	323	310

Supplementary Note 6. The theoretical formulas of optical properties[17–19].

The averaged transmittance and reflectance in the visible (0.38–0.78 μm) and solar (0.38–2.5 μm) spectra, respectively, were calculated as follows:

$$T_{\text{vis}} = \int_{0.38\ \mu\text{m}}^{0.78\ \mu\text{m}} T(\lambda) \cdot I_{\text{AM1.5}}(\lambda) d\lambda \Big/ \int_{0.38\ \mu\text{m}}^{0.78\ \mu\text{m}} I_{\text{AM1.5}}(\lambda) d\lambda \tag{29}$$

$$T_{\text{sol}} = \int_{0.38\ \mu\text{m}}^{2.5\ \mu\text{m}} T(\lambda) \cdot I_{\text{AM1.5}}(\lambda) d\lambda \Big/ \int_{0.38\ \mu\text{m}}^{2.5\ \mu\text{m}} I_{\text{AM1.5}}(\lambda) d\lambda \tag{30}$$

$$R_{\text{vis}} = \int_{0.38\ \mu\text{m}}^{0.78\ \mu\text{m}} R(\lambda) \cdot I_{\text{AM1.5}}(\lambda) d\lambda \Big/ \int_{0.38\ \mu\text{m}}^{0.78\ \mu\text{m}} I_{\text{AM1.5}}(\lambda) d\lambda \tag{31}$$

$$R_{\text{sol}} = \int_{0.38\ \mu\text{m}}^{2.5\ \mu\text{m}} R(\lambda) \cdot I_{\text{AM1.5}}(\lambda) d\lambda \Big/ \int_{0.38\ \mu\text{m}}^{2.5\ \mu\text{m}} I_{\text{AM1.5}}(\lambda) d\lambda \tag{32}$$

where $T(\lambda)$ and $R(\lambda)$ are the transmissivity and reflectivity as a function of wavelength (μm), respectively, $I_{\text{AM1.5}}(\lambda)$ is the standard solar spectral irradiance spectra for air mass 1.5. The ΔT_{vis} and ΔT_{sol} were calculated with the formulas:

$$\Delta T_{\text{vis}} = T_{\text{vis-H}} - T_{\text{vis-C}} \tag{33}$$

$$\Delta T_{\text{sol}} = T_{\text{sol-H}} - T_{\text{sol-C}} \tag{34}$$

where, $T_{\text{vis-H}}$ and $T_{\text{vis-C}}$ are the visible transmissivity in heating and cooling modes, respectively; $T_{\text{sol-H}}$ and $T_{\text{sol-C}}$ are the solar transmissivity in heating and cooling modes, respectively. Similarly, the average emissivity in long-wave infrared (LWIR; 2.5–20 μm) can be defined as:

$$\varepsilon_{\text{LWIR}} = \int_{2.5\ \mu\text{m}}^{20\ \mu\text{m}} \varepsilon(\lambda, T) \cdot I_{\text{BB}}(\lambda, T)\, d\lambda \Big/ \int_{2.5\ \mu\text{m}}^{20\ \mu\text{m}} I_{\text{BB}}(\lambda, T)\, d\lambda \tag{35}$$

where, $\varepsilon(\lambda,T)$ is emissivity as a function of wavelength (μm), $I_{\text{BB}}(\lambda,T)$ is the spectral irradiance of a blackbody at a certain temperature. The $\varepsilon_{\text{LWIR}}$ spectral profile was plotted according to the Kirchhoff's law of thermal radiation: $\varepsilon(\lambda) = A(\lambda) = 1 - T(\lambda) - R(\lambda)$, here $R(\lambda)$ is the spectral LWIR reflectance and $T(\lambda)$ is the spectral LWIR transmittance, as measured by Fourier-transform infrared spectroscopy. The $\Delta\varepsilon_{\text{LWIR}}$ was calculated with the formula:

$$\Delta\varepsilon_{\text{LWIR}} = \varepsilon_{\text{LWIR-C}} - \varepsilon_{\text{LWIR-H}} \tag{36}$$

where, $\varepsilon_{\text{LWIR-H}}$ and $\varepsilon_{\text{LWIR-C}}$ are the integrated LWIR emissivity of window samples in heating and cooling modes, respectively.

Supplementary References

1. Yeang, A. L. *et al.* Transparent, high-charge capacity metal mesh electrode for reversible metal electrodeposition dynamic windows with dark-state transmission <0.1%. *Adv. Energy Mater.* **12**, 2200854 (2022).
2. Li, H., Zhang, W. & Elezzabi, A. Y. Transparent zinc-mesh electrodes for solar-charging electrochromic windows. *Adv. Mater.* **32**, 2003574 (2020).
3. Deru, M. *et al*. *Commercial Reference Building: Medium Office*. [Data set]. Open Energy Data Initiative (OEDI). National Renewable Energy Laboratory. (2014).
4. Shao, Z. Tri-band electrochromic smart window for energy savings in buildings. *Nat. Sustain.* **7**, 796–803 (2024).
5. Zhao, X. *et al.* Dynamic glazing with switchable solar reflectance for radiative cooling and solar heating. *Cell Rep. Phys. Sci.* **3**, 100853 (2022).
6. Rao, Y. *et al.* Ultra-wideband transparent conductive electrode for electrochromic synergistic solar and radiative heat management. *ACS Energy Lett.* **6**, 3906–3915 (2021).
7. Sui, C. *et al.* Dynamic electrochromism for all-season radiative thermoregulation. *Nat. Sustain.* **6**, 428–437 (2023).
8. Ergoktas, M. S. *et al.* Multispectral graphene-based electro-optical surfaces with reversible tunability from visible to microwave wavelengths. *Nat. Photonics* **15**, 493–498 (2021).
9. Jia, Y. *et al.* Transparent dynamic infrared emissivity regulators. *Nat. Commun.* **14**, 5087 (2023).
10. Deng, Y. *et al.* Annual energy-saving smart windows with actively controllable passive

radiative cooling and multimode heating regulation. *Adv. Mater.* **36**, 2401869 (2024).

11. Huang, Y. *et al.* A novel liquid flow electrochromic smart window for all-year-round dynamic photothermal regulation. *Energy Environ. Sci.* **18**, 1824–1834 (2025).
12. Gliah, O., Kruczek, B., Etemad, S. Gh. & Thibault, J. The effective sky temperature: an enigmatic concept. *Heat Mass Transf.* **47**, 1171–1180 (2011).
13. Berdah, P. & Fromberg, R. The thermal radiance of clear skies. *Sol. Energy* **29**, 299–314 (1982).
14. Negev, E. *et al.* Algae Window for reducing energy consumption of building structures in the Mediterranean city of Tel-Aviv, Israel. *Energy Build.* **204**, 109460 (2019).
15. ISO 15099:2003-Thermal performance of windows, doors and shading devices–Detailed calculations.
16. Xue, P. *et al.* Secondary solar heat gain modelling of spectral-selective glazing based on dynamic solar radiation spectrum. *Build. Simul.* **16**, 2211–2224 (2023).
17. Zhang, Q. *et al.* Daytime radiative cooling dressings for accelerating wound healing under sunlight. *Nat. Chem. Eng.* **1**, 301–310 (2024).
18. Wang, S. *et al.* Scalable thermochromic smart windows with passive radiative cooling regulation. *Science* **374**, 1501–1504 (2021).
19. Lin, C. *et al.* All-weather thermochromic windows for synchronous solar and thermal radiation regulation. *Sci. Adv.* **8**, eabn7359 (2022).